

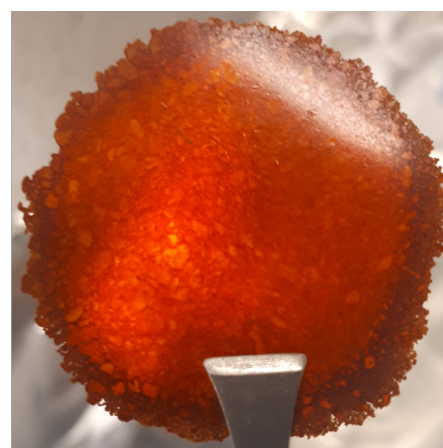
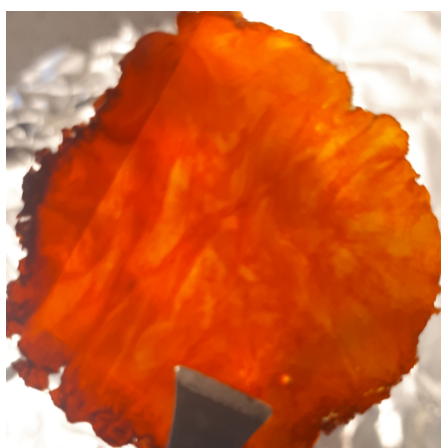
Nora Statle Løndal

Effects of material structure on the electrical properties of ferroelectric plastic crystal tetramethylammonium bromotrichloroferrate(III)

Master's thesis in Nanotechnology

July 2020

NTNU
Norwegian University of Science and Technology
Faculty of Natural Sciences
Department of Materials Science and Engineering



Effects of material structure on the electrical properties
of ferroelectric plastic crystal tetramethylammonium
bromotrichloroferrate(III)


NORA STATLE LØNDAL

SPRING 2020

TMT4910 NANOTECHNOLOGY

MASTER THESIS

SUPERVISOR:
PROF. MARI-ANN EINARSRUD
CO-SUPERVISOR:
DR. JULIAN WALKER
SUBMITTED:20.07.2020

 **NTNU**
Norwegian University of Technology and Science
Department of Materials Science and Engineering

Preface

This thesis is part of the course TMT4910 Nanotechnology, Master thesis. The work is a continuation of the work carried out in the course TMT4510 Nanotechnology Specialisation project, which is described in the report: Improving synthesis of ferroelectric plastic crystal tetramethylammonium bromotrichloroferrate [1].

The Covid-19 pandemic has influenced society on a global scale in the period working on this thesis and has impacted lab work, training on new instruments, supervision and the general everyday situation. I want to give a special thank you to NTNU senior engineer Johannes Ofstad who has carried out the experimental work related to Infrared Spectroscopy, as I was not allowed training on new instruments, and helped with CRR processing of the Raman data, as I did not have access to the required software from home office. My supervisor Prof. Mari-Ann Einarsrud and co-supervisor Dr. Julian Walker have made great effort to supervise me through various channels, I appreciate all your help and guidance greatly. Finally I want to thank my family and friends for support during this time. My parents were true heroes while I was back home for the better part of three months and my boyfriend should have a diamond decorated platina medal for all the hours spent on videochat.

"IN THIS short historical survey, I hope to give, to the best of my ability, the early experimental evidence concerning plastic crystals, and I apologize in advance if there remain some important gaps in my text, since I am a specialist in the study of physical properties of organic compounds, but am not so learned, either in inorganic chemistry or in theoretical physics"

-Professor J. Timmermanns

Abstract

Ferroelectrics are desirable for a range of applications including mobile phones, medical ultrasound and digital memory, due to their switchable electrical polarisation. Metal oxides which govern the current market of ferroelectrics perform appropriately in a multitude of applications, but their prevailing requirement for high processing temperatures and generally brittle nature, demand high production energy and confine their compatibility in next generation electronics. Plastic crystals possess a plastic crystal mesophase that enables moderate temperature processing and shaping. A number of plastic crystals, like tetramethylammonium bromotrichloroferate(III): $[(\text{CH}_3)_4\text{N}]^+[\text{FeBrCl}_3]^-$ (TMABrFeCl₃), hold stable ferroelectric phases at roomtemperature, which encourage to explore plastic crystals ferroelectrics as a sustainable, light weight and shapeable option. The goal of this study was to gain insight on the structure-property relationship of plastic crystal ferroelectrics through a study of the synthesis-structure-property relationships of TMAFeBrCl₃. To achieve this, three substudies were carried out on pressed agglomerate and pressed powder TMAFeBrCl₃ samples. This includes a study of microstructure by optical imaging and scanning electron microscope (SEM), structural phase determination using X-ray diffraction (XRD), differential scanning calorimetry (DSC) and vibrational spectroscopy, as well as, characterisation of the materials functional properties through current-voltage measurements and field dependent hysteresis behaviour. Optical imaging propose grain size difference between the different samples, but SEM shows no microstructural difference between them. Structural phase determination reveals structural difference, in terms of the pressed powder samples being more susceptible to end up having the non-ferroelectric Cmcm as majority phase than the pressed agglomerate samples. Characterisation of electrical properties shows that all samples exhibit typical ferroelectric behaviour, indicating that the Cmcm phase majority samples must experience a field induced phase transition into the ferroelectric Amm2 phase.

Sammendrag

Ferroelektriske materialer er foretrukne i en rekke applikasjoner, slik som mobiltelefoner, medisinsk ultralyd og digitalt minne, på grunn av at de har elektrisk polarisasjon som kan endre retning. Metalloksider, som er ledende på det ferroelektriske markedet, fungerer hensiktsmessig i mange applikasjoner, men det at de har et behov for høye prosesseringstemperaturer samt at de generelt er skjøre, gjør at det er begrenset hvor kompatible de er med neste generasjon av elektronikk. Plastiske krystaller har en plastisk mesophase som gjør prosessering og forming mulig ved moderate temperaturer. Et antall plastiske krystaller, slik som for eksempel tetrametylammonium-bromotrikloroferrat(III): $[(\text{CH}_3)_4\text{N}]^+[\text{FeBrCl}_3]^-$ (TMAFeBrCl₃), har stabile ferroelektriske faser ved romtemperatur. Dette oppmuntrer til å utforske muligheten til å bruke ferroelektriske plastiske krystaller som et alternativ til de konvensjonelle metalloksidene. Målet med denne studien var å oppnå innsikt i hvordan egenskapene til plastiske krystaller avhenger av strukturelle faktorer, ved å studere forholdet mellom synteseforhold, struktur og egenskaper i den plastiske krystallforbindelsen TMAFeBrCl₃. For å oppnå dette ble tre understudier utført på pressede agglomerater og presset pulver av den aktuelle forbindelsen. Dette innebærer en studie av mikrostruktur ved optiske bilder og sveipelektronmikroskopi (SEM), bestemmelse av strukturell fase ved røntgendiffraksjon (XRD), differensiell skanningskalorimetri (DSC) og vibrasjonsspektroskopi, samt karakterisering av materialets funksjonelle egenskaper gjennom måling av strøm som funksjon av spenning, samt analyse av feltavhengige hysteresekurver. Fra optiske bilder tyder det på at kornstørrelsen er forskjellig i de ulike pressede prøvene, men SEM viste ingen mikrostrukturell forskjell mellom dem. Fasebestemmelsene avslører at det er strukturelle ulikheter, i form av at prøvene presset fra pulver er mer utsatt for å ende opp med å ha den ikke-ferroelektriske C_mc_m-fasen som hovedfase enn prøvene presset fra agglomerater. Karakterisering av elektriske egenskaper viser at alle prøvene har typisk ferroelektrisk karakteristik, noe som tyder på at C_mc_m-fasen gjennomgår en feltindusert faseovergang til den ferroelektriske fasen Amm2.

Contents

| | Page |
|---|-----------|
| List of abbreviations | 13 |
| 1 Background | 15 |
| 1.1 Motivation | 15 |
| 1.2 Aim | 16 |
| 2 Introduction | 19 |
| 2.1 Ferroelectrics | 19 |
| 2.1.1 A ferroelectric material | 19 |
| 2.1.2 Polarisation | 20 |
| 2.1.3 Characteristic field dependent behaviour | 22 |
| 2.2 Fracture surfaces and grain size determination | 26 |
| 2.3 Plastic Crystals | 27 |
| 2.3.1 Ferroelectric plastic crystals | 28 |
| 2.4 Tetramethylammonium bromotrichloroferrate(III) | 29 |
| 2.4.1 Structure and crystallographic phases | 29 |
| 2.4.2 Synthesis and processing | 30 |
| 2.4.3 Vibrational spectroscopy | 31 |
| 2.4.4 Electrical properties | 31 |
| 3 Experimental | 33 |
| 3.1 Synthesis of tetramethylammonium bromotrichlorideferrate(III) crystals by slow evaporation from water | 33 |
| 3.2 Pressing of polycrystalline samples | 33 |
| 3.3 Characterisation | 35 |
| 3.3.1 Crystal microstructure | 35 |
| 3.3.2 Crystallographic structures | 35 |
| 3.3.3 Vibrational spectroscopy | 35 |
| 3.3.4 Phase transitions | 36 |
| 3.3.5 Electrical properties | 37 |
| 4 Results | 39 |
| 4.1 Observation upon synthesis and pressing | 39 |
| 4.2 Sample microstructures | 40 |
| 4.3 Crystallographic information of crystal powder and pressed samples | 45 |
| 4.4 Vibrational spectroscopy | 47 |
| 4.4.1 Raman | 47 |
| 4.4.2 Infrared spectroscopy | 49 |
| 4.5 Phase transitions | 50 |
| 4.6 Results from I-V measurements and P-E, I-E and S-E hysteresis measurements | 53 |
| 4.6.1 Current-voltage data | 53 |
| 4.6.2 Polarisation, current density and strain loops | 55 |

| | |
|---|-----------|
| 5 Discussion | 59 |
| 5.1 Sample microstructure | 59 |
| 5.2 Characterisation of majority phase | 60 |
| 5.3 Electrical properties | 62 |
| 6 Conclusion | 65 |
| 7 Further work | 67 |
| Appendices | 71 |
| A Complementary figures | 73 |
| A.1 CRR processing of Raman data | 73 |
| A.2 P-E, I-E and S-E hysteresis curves at maximum field | 74 |
| B Risk assessment | 76 |

List of abbreviations

| | |
|------------------------|---|
| CH ₃ | methyl |
| E _c | coersive field |
| FeBrCl ₃ | bromotrichloroferrate(III): [FeBrCl ₃] ⁻ |
| I _{La} | leakage current density after |
| I _{Lb} | leakage current density before |
| I _{Peak} | maximum current density |
| P _r | remnant polarisation |
| S _{PP} | peak-to-peak strain |
| TMAFeBrCl ₃ | tetramethylammonium bromotrichloroferrate(III): [(CH ₃) ₄ N] ⁺ [FeBrCl ₃] ⁻ |
| TMAFeCl ₃ | tetramethylammonium tetrachloroferrate(III): [(CH ₃) ₄ N] ⁺ [FeCl ₄] ⁻ |
| ATR | attenuated total reflectance |
| BTO | barium titanate: BaTiO ₃ |
| CCDC | Cambridge crystallographic data center |
| CRR | cosmic ray removal |
| DSC | differential scanning calorimetry |
| FTIR | Fourier transformation infrared |
| FWHM | full width at half maximum |
| IR | infrared |
| MEMS | micro electromechanical systems |
| PZT | lead zirconate titanate: Pb[Zr _x Ti _{1-x}]O ₃ |
| SEM | scanning electron microscope |
| TMA | tetramethylammonium: [(CH ₃) ₄ N] ⁺ |
| TMABr | tetramethylammonium bromide: (CH ₃) ₄ NBr |
| XRD | X-ray diffraction |

1 Background

1.1 Motivation

Ferroelectric materials are characterised by their switchable and spontaneous polarisation, their piezoelectric coefficients, as well as their dielectric properties[2, 3]. This makes them useful in a range of electronic application such as transducers, actuators, sensors and capacitors. The materials that govern as ferroelectrics in today’s technologies are metal oxides such as barium titanate: BaTiO_3 (BTO) and lead zirconate titanate: $\text{Pb}[\text{Zr}_x\text{Ti}_{1-x}]\text{O}_3$ (PZT). These were discovered in the 1940s and 1950s, respectively, after which both grew in commercial significance and still dominate the ferroelectric material markets today. However, in the search for materials that are compatible with next generation electronics, qualities such as low energy consumption, high flexibility, ease of processing and sustainable products are sought after. These are qualities the metal oxides often lack, as they are known to be rigid, brittle and need high temperature processing. So, as society strives to engage in longstanding sustainable solutions, alternatives to the conventional ferroelectrics are needed. Therefore, organic-inorganic hybrid plastic crystal ferroelectrics, a novel group of materials, that offer a shapeable, lightweight and flexible alternative to metal oxide ferroelectrics have gained attention. In addition to their promising functional properties, plastic crystals can be crystallised from aqueous solutions without the need for organic solvents and can be plastically deformed at moderate temperatures, providing a non-technically demanding and cost effective pathway for material synthesis.

Materials referred to as plastic crystals are defined by their possession of a moderately high temperature mesophase before their melting point. The mesophase is an intermediate solid-liquid state in which the molecule is fixed at a given position in the crystal lattice, but can rotate in this position. This state facilitates plastic deformation. Such plastic crystal mesophases most often occur in supramolecular materials made from globular molecules [4]. This means that the material has molecular ion constituents and not single elements, which is common for metal oxide ferroelectrics. When molecular ion constitutes build a material, the options for its sustainable development widens in terms of tailoring material properties without increasing the elemental footprint. The elemental footprint is the number of periodic table elements that are added to the composition, as well as what effect the usage of certain element has, both on the environment and related to ethics, in terms of mining, abundancy, recycling, disposal, toxicity and more [5]. The same set of elements can create a range of different molecules or ions and a large variety of properties might be achieved without increasing the amount of periodic table elements put into the composition. In fact, nature itself uses only a few very abundant elements such as carbon, oxygen and hydrogen to make all its creations. Can we make sustainable yet specialised materials the same way?

Sustainability is key when developing next generation materials for electronics. Decarbonising is an important aspect in this and the carbon footprint related to producing ferroelectrics needs to be reduced [7]. One way of reducing the carbon footprint is to reduce the energy consumption associated with production. High temperature processing requires large amounts of energy, and thus, being able to reduce the processing temperature can possibly reduce the energy consumption and the carbon footprint considerably. Plastic crystals, being shapeable at temperatures as low as around $120\text{ }^\circ\text{C}$, opens for large reductions. This will also give positive outcome in terms of lowering the production cost of the ferroelectrics. A third major benefit of reduced production temperature is that the materials will be more compatible with other material systems of electronic devices, that does not comply well with the high processing temperatures of conventional ferroelectrics [8,

9]. Future technologies also include further development of flexible electronics, including energy harvesting devices, electronic textiles, flexible displays (Figure 1.1) and micro electromechanical systems (MEMS) [10], which all are technologies that potentially could utilise plastic crystals.

A promising example of a plastic crystal that is ferroelectric is tetramethylammonium bromotrichloroferrate(III): $[(\text{CH}_3)_4\text{N}]^+[\text{FeBrCl}_3]^-$ (TMAFeBrCl₃). The compound, which is composed of organic cations and inorganic complex anions, shows multiple phase transitions over a range of temperatures. At room temperature it is ferroelectric, while at higher, yet moderate temperatures, the material takes on a shapeable plastic crystal phase. The compound can be achieved by simple synthesis through solution precipitation of crystals from water upon dehydration.

Even though a few compounds, such as TMAFeBrCl₃, have been recognised, the essential principles creating the foundation for their composition-structure-property relationship are not yet known. Therefore more comprehensive studies of the structure, properties and even synthesis of such materials are required to explore the full potential of these interesting materials. One such potential lies in the ability to tailormake compounds by using abundant and sustainable building blocks. Tailoring materials with specific properties by choosing the right constituents is a strategy commonly used in material science[5]. For plastic crystals, due to having molecular or ion constituents, it should be possible to custom-make material properties while avoiding increasing the elemental footprint. However, the molecular species in plastic crystals are dynamic and exhibit different degrees of rotational freedom for different temperatures and crystal structures. Thus, in order to understand how one can tailor the properties of the plastic crystals ferroelectrics, a better understanding of the influence of molecular charge, size and dynamics on the functional properties, is necessary. Another factor that is known to have profound effect on the functional properties of conventional ferroelectric, is their microstructure [11–14]. The relationship between microstructure and properties in plastic crystal ferroelectrics is completely unexplored.

1.2 Aim

The scope of the study is to illuminate the synthesis-structure-property relationships of TMAFeBrCl₃ and in doing so give new insight on the structure-property relationships in the whole class of plastic crystal ferroelectrics. The aim is to investigate the synthesis-structure-property relationship of the promising ferroelectric plastic crystal TMAFeBrCl₃ through three distinct substudies, which will be carried out on two types of hot pressed samples where the grain size is expected to differ. First, by a study of sample microstructure conducted by inspecting optical images of the pressed sam-

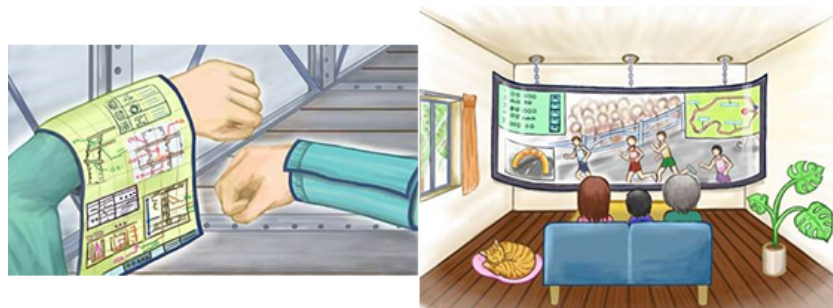


Figure 1.1: Possible application of TMAFeBrCl₃ plastic crystals are in flexible displays. Illustrative images from [6]

ple surfaces and SEM micrograph of fracture surfaces from the pressed samples. Second, through determining the structural phase composition of the pressed samples by X-ray diffraction (XRD) and Rietvelt-refinement, as well as supporting data from differential scanning calorimetry (DSC), Raman and infrared (IR) spectroscopy. Finally, electrical measurements, including current-voltage and field dependent hysteresis data, will collect information about the materials functional properties, which is hypothesised to correlate to the microstructural and phase compositional results.

2 Introduction

This thesis treats the synthesis and characterisation of the ferroelectric plastic crystal TMAFeBrCl_3 . To make the reader familiar with the topic the introduction will touch upon relevant topics organised in the following subheadings: Ferroelectrics, Plastic Crystals and Tetramethylammonium bromotrichloroferrate(III).

2.1 Ferroelectrics

2.1.1 A ferroelectric material

A material that, below its Curie temperature, possess a polarisation which is spontaneous and switchable when applying an electrical field (Figure 2.1) is known as a ferroelectric [3]. A number of various chemical compounds are classified as ferroelectrics, and their ferroelectric properties are caused by a selection of diverse crystallographic features [15]. In spite of that, one of the main fundamental causes of these properties is briefly described as atom displacement, which facilitate an alteration of a symmetrical environment into a non-symmetric one and, thereby, lead internal dipoles to assemble. The materials crystal structure will solely affect said property.

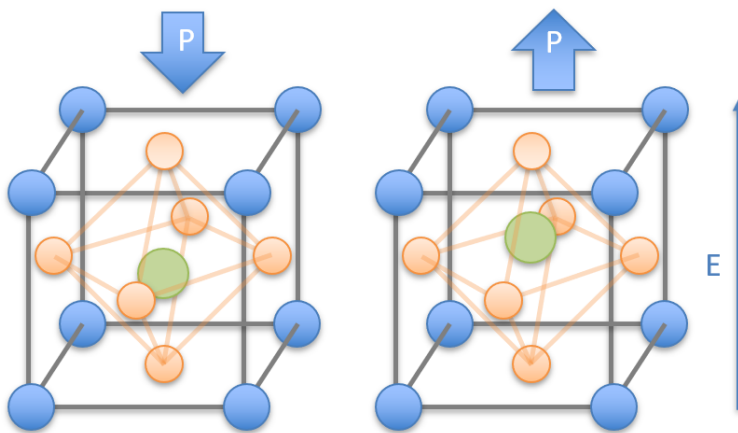


Figure 2.1: A material that, below its Curie temperature T_c , possess a polarisation that is spontaneous and switchable, due to atom displacement that cause internal dipole formation, when applying an electrical field is know as a ferroelectric [3]. Retrieved from [1].

There are in total 233 possible space groups which are classified into 32 crystalline classes (Figure 2.2). These classes are subdivided into seven crystal systems, which by decreasing symmetry are mentioned as follows; cubic, hexagonal, trigonal, tetragonal, orthorombic, monoclinic and triclinic [2]. In Figure 2.2 one can see that 11 of the crystal classes are centrosymmetric, and the rest are non-centrosymmetric. Looking at the non-centrosymmetric classes, 20 are piezoelectric. This is explained as surface charges are being able to form, in the material, as a reaction to external stress being applied, as well as the reverse scenario where applying an external electric field induce stress in the material. Out of the 20 piezoelectric crystalline classes, there are ten pyroelectric ones, in which a change in the spontaneous polarisation is occurring as a response to a temperature change. Lastly, and most importantly for this thesis, is the subset of pyroelectric materials that are ferroelectric and thus, as earlier mentioned, exhibit a switchable spontaneous polarisation in reaction to an externally applied electric field.

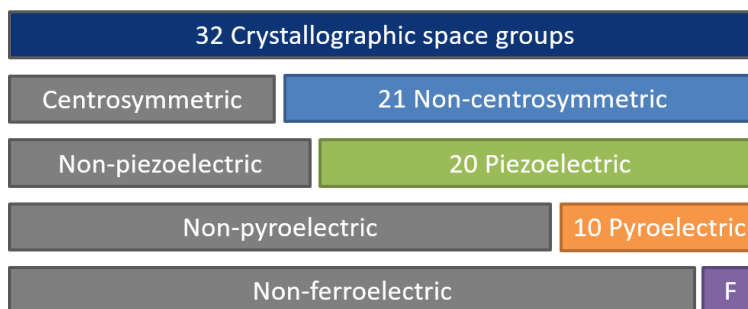


Figure 2.2: Space groups: In total, 32 crystalline space groups exist. Out of these, 21 are non-centrosymmetric, and all but one are piezoelectric. Half of the piezoelectric space groups are pyroelectric and a few of these are ferroelectric, which is marked as "F" in the purple box in this Figure. Retrieved from [1].

2.1.2 Polarisation

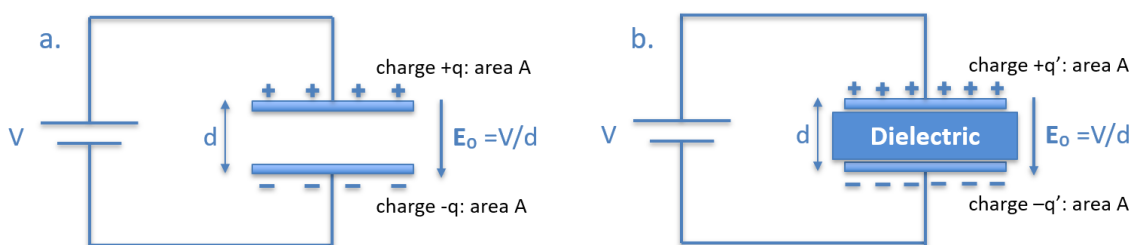


Figure 2.3: For a parallel plate capacitor accumulation of charge will occur on the two parallel plates when applying a voltage, V (a). If a slab of dielectric material substitutes the vacuum, a change in the charges on the parallel plates will happen. Retrieved from [1].

An essential concept regarding ferroelectrics is polarisation and this can be understood by what happens in a parallel plate capacitor. If a dielectric material is exposed to an external electrical field, \mathbf{E}_0 , in the same way the dielectric in a capacitor is (Figure 2.3), atoms, ions and molecules of the dielectric will be polarised [15]. This makes internal electric dipoles, with dipole moment \mathbf{p} , that point from negative to positive charge, form (Figure 2.4). Every single component within the material will hold an induced dipole moment, typically proportional to the electrical field that is applied to the polarisability. However, the local field is not the same as the applied electrical field, \mathbf{E}_0 , because contributions from permanent or temporary dipoles in the structure will also contribute to the active local field. The total of all the dielectric components will cause the opposite surfaces of the solid to be charged positively and negatively, rising a net polarisation \mathbf{P} , also pointing from negative to positive charge [15]. If the material is isotropic, \mathbf{P} will be both proportional and parallel to \mathbf{E}_0 at normal field strengths. For cubic crystal structures a directional dependence between the applied electrical field and the relative permittivity is not present. For lower symmetry crystal systems there is, however, such a directional dependence [15]. But in polycrystalline materials this directional dependence is not noticed after all, as the crystallographic symmetry is averaged by the random orientation of the crystalline grains. Thus, defects, such as point defects, grain boundaries and mobile charge carriers, in the polycrystalline materials affect the relative permittivity more strongly than the fundamental symmetry characteristics of the crystals.

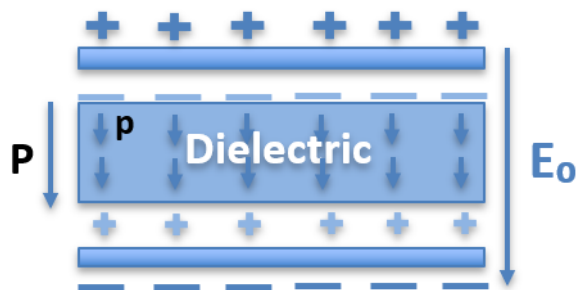


Figure 2.4: Polarisation of a dielectric: Surface charge is achieved when an external electrical field, \mathbf{E}_0 is applied to the dielectric. This happens because internal dipoles, \mathbf{p} , form and induce an observable polarisation \mathbf{P} [15]. Retrieved from [1].

In a typical dielectric material the observed polarisation at zero applied field is zero [15], but in piezoelectrics this is not the case. For piezoelectric materials, mechanical stress such as pressure can induce electrical surface charge independently. Also, if an electrical field was to be applied to such a material, the shape of it would change, meaning that the piezoelectric effect is reversible. In a pyroelectric material, where polarisation happens when a temperature change creates internal dipoles and a change in atomic positions, polarisation can be present without application of either electrical field or mechanical stress. The polarisation is then said to be spontaneous and is denoted by \mathbf{P}_s . Ferroelectrics, which are a subset of the ferroic material groups mentioned above, also carry a spontaneous polarisation. What characterise the ferroelectrics specifically, is that by applying an external electrical field, the spontaneous polarisation can be switched. Additional criteria to be a good ferroelectric include having good insulating properties, so that they are efficient and have low electrical loss.

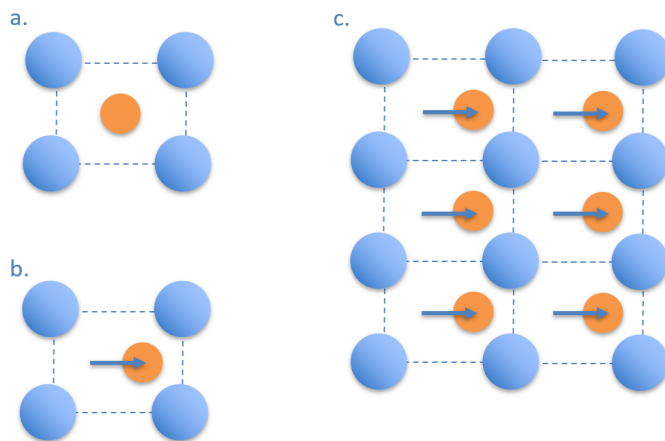


Figure 2.5: (a.) A unit cell with cation in the centre. (b.) A unit cell with cation shifted so that it forms an electric dipole. (c.) An unit cell array, creating a ferroelectric structure. Retrieved from [1]

Like previously mentioned, a basic mechanism causing ferroelectricity withing materials is that a symmetric environment is shifted into a antisymmetric one due to displacement of atoms within the material structure [15]. In Figure 2.5 this is illustrated by the simple two dimensional model of a rectangular array of anions with cations located in the centre (Figure 2.5 a), and thus aligning with the mass centres of the array of anions. This yields a symmetric and non-ferroelectric environment.

If the cation are shifted slightly off the centre of the anion arrangement, the structure will achieve stability, but the cation and anion mass centres will no longer line up, and a dipole is formed (Figure 2.5 b). The same will happen in each unit of the whole structure, and collectively they yield a full structure of aligned dipoles (Figure 2.5 c). In a typical ferroelectric a cation displacement in two or more energetically equivalent directions is allowed. When the cation is shifted, the structure is stable, meaning that a energy minimum is achieved. In the discussed model, two such minima will be present, while the anion mass centre position will act as a energy barrier between the two. Cations that are close to each other will typically, due to local interactions, take the same displacement. This leads to a local volume of parallel dipoles, and thus a uniform direction of polarisation, being formed within a ferroelectric structure. Volumes like that, holding a specific orientation, are known as domains. A boundary between two domains with different polarisation direction is called domain walls.

2.1.3 Characteristic field dependent behaviour

P-E hysteresis loops

The domains in a ferroelectric crystal will typically be distributed equally between the allowed directions of polarisation of the given crystal symmetry, resulting in an overall polarisation of zero [14, 15]. In Figure 2.6 one can see how a typical ferroelectric will behave in terms of polarisation as a function of applied electrical field. The material will behave as a normal dielectric if only a small electrical field is applied, corresponding to region O-A, as the electrical field applied is not large enough to surmount the energy barrier that separates the shifted configurations available. Whenever the field strength is raised, energy will be transferred to the cations which at some point will manage to overcome the energy barrier, and the cation displacement will bring the orientation of electric dipoles to change. The domains will continue to progressively shift their orientation, making the observed polarisation of the material to build rapidly (region A-B). When all dipoles are parallelly aligned, the crystal will in simple terms act as one single domain, and a saturated state is obtained (region B-C).

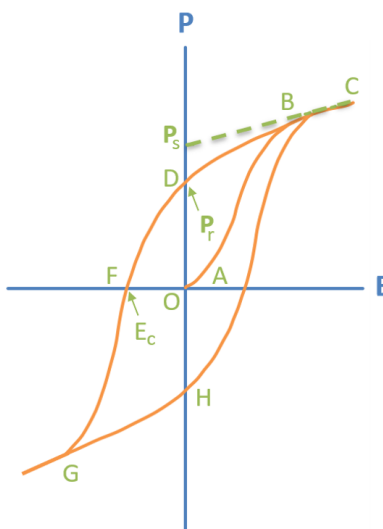


Figure 2.6: Hysteresis behaviour of polarisation, \mathbf{P} , as a function of applied electrical field \mathbf{E} is characteristic of a ferroelectric. Retrieved from [1]

If a reversal of the applied field is employed, it would be necessary to supply additional energy to recreate numerous domains, making the trace of the P-E-curve to be changed from the one followed during initial application of the field. Steadily the dipoles will rearrange their direction so that they trace through B-D-F and finally the material will reach a new state of saturation in G. If the field is applied in the original direction once more, another rearrangement of the dipoles will occur making them switch back such that they trace along G-H-C. The closed P-E-curve that will be achieved, termed hysteresis loop, is a core characteristic of ferroelectrics termed a hysteresis loop. The value of O-D is known as the remnant polarisation (P_r), and the value of O-F is recognised as the coercive field E_c , which typically range between 10-100 V. By linearly extrapolating the saturated state(B-C) onto the y-axis, for example at $E=0$, one achieves the spontaneous polarisation, P_s . The coercive field (E_c) can also be found through the current density I . Polarisation and current density is related by $I = \frac{dP}{dt}$ and E_c gives maximum current density (I_{Peak}) [16]. In Figure 2.7 the relation between the P-E and I-E hysteresis loops are shown.

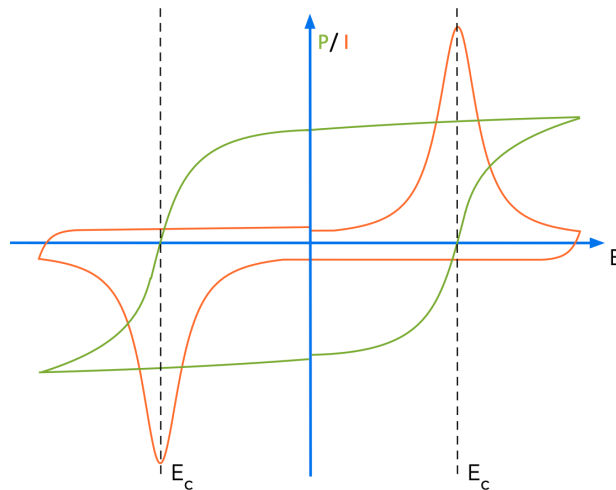


Figure 2.7: Current density I is related to polarisation P through $I = \frac{dP}{dt}$. I is maximum at E_c . Hysteresis behaviour of polarisation, P , as a function of applied electrical field E is characteristic of a ferroelectric. Figure inspired from Fig.7 in [16].

S-E hysteresis loops

The characteristic P-E behaviour of the ferroelectrics are accompanied by distinctive strain-electric field hysteresis [3]. The strain-field behaviour is yielded by mainly three effects, being domain wall switching and movement, in addition to the converse piezoelectric effect belonging to the lattice. The ferroelectric S-E curves are recognised by their butterfly alike shape (Figure 2.8). When zero field is applied, the strain is also zero (A). If one applies an electrical field in the same direction that the spontaneous polarisation is pointing, and the field is increased, the material crystal will expand in response to the piezoelectric effect so that the strain will trace through A-B-C until a maximum field is reached at C. The decrease of the field will be initialised at C but its direction will be maintained in the polarisation direction. The strain will trace the same path, in opposite direction, back to A. Next, the field direction will be switched making a contraction occur in the crystal making the strain grow positively until D where the strain will be sufficiently large to switch the polarisation direction, making it parallel to the electrical field. The strain will then again be turned positive in E. As one continuous to drive the field to larger negative values, the strain will

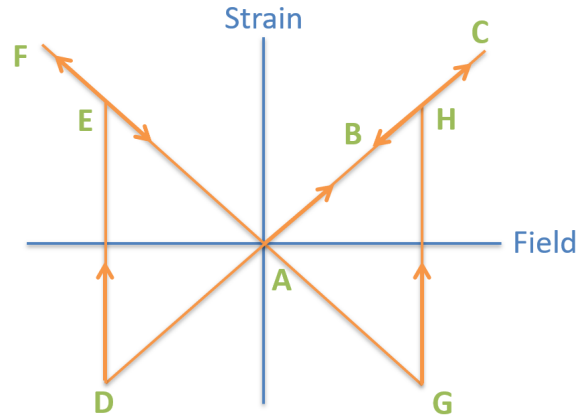


Figure 2.8: An ideal strain-field hysteresis loop of a ferroelectric crystal where the polarisation can be switched by 180 degrees only [3]. The loop resembles a butterfly. Retrieved from [1]

reach F, before decreasing towards A as the field is lowered. At G the polarisation is reversed, giving an abrupt change in the strain. Apart from in D and G, the strain-field relationship will be linear in an idealised model. Meaning that, except for in D and G, the strain is solely employed by the piezoelectric effect. However, this relationship is in truth more complicated, as factors such as the domain wall motion is not added to the idealised model.

Footprint of material properties in hysteresis loop

The ideal models for the P-E behaviour described above yield symmetric hysteresis loops, giving the value of E_c and P_r equal on both positive and negative side. The reality is however that the hysteresis loops are affected by a range of factors such as domain wall motion, material composition, sample thickness, thermal processing, mechanical stress, charged defects present in the material, etc[14, 15]. Thus, the hysteresis loops can be used to gain information about material properties and structure. The most obvious properties you can gain from a hysteresis loops are E_c and P_r , but these will vary depending factors such as material type and grain size.

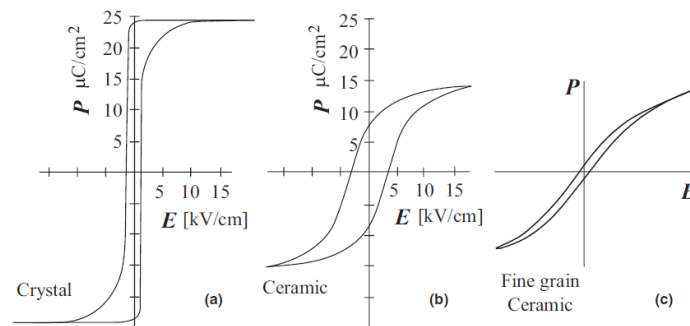


Figure 2.9: Polarisation-field hysteresis loops for BTO with various grain sizes at room temperature. (a) Single crystal BTO (b) Coarse grained polycrystalline BTO (c) Fine grained polycrystalline BTO. Retrieved from [14].

Generally P_r for bulk perovskite material lie in the range of 0.2-0.5 C/m², while the coercive field can range between 0.5-150 kV/cm [14]. Comparing single crystal compound to polycrystalline ceramic materials of the same composition, large variation is observed, mainly due to pinning at domain walls. In Figure 2.9 one can observe the difference between single crystal, coarse grained and fine grained polycrystalline BTO. This shows that the single crystal material hysteresis (2.9 a) is squared with a small E_c and large P_r , while in the ceramic coarse grained BTO (2.9 b) the hysteresis loop is more slanted with larger E_c and lower P_r . With smaller grain size, in the fine grained BTO ceramic, the effect is amplified (2.9 c). That we see more ease of domain wall switching, given by E_c , in the single crystal material can be explained by the lack of domain wall pinning at grain boundaries. Similarly can the amplification of the effect with decreasing grain size be explained by increasing grain boundary area. In addition a lower percentage of the domains will be able to be polarised in a polycrystalline ferroelectric with random distribution of domain polarisation, explaining the lowering of P_r , compared to in a single crystal ferroelectric of same composition. The lowering of P_r is stated to be more strict than the increase of E_c with decreasing grain size.

A field induced phase transition will also make an impact on the hysteresis loops. A double P-E curve (Figure 2.10 a) can be observed if a antiferroelectric structure is applied a large enough field to cause macroscopic polarisation to occur [14, 17]. As the applied field is increased to a E_f an antiferroelectric-ferroelectric field induced transition will take place, and lead to a rapid increase in polarisation, corresponding to the polarisation of the ferroelectric structure. Similarly, the polarisation will rapidly drop as the field is lowered below the critical field E_a . The effect will also be observed in the negative part of the loop. For this to happen the free energy of the antiferroelectric state needs to be slightly lower than the ferroelectric state. The field induced transition is also evident in I-E curves (Figure 2.10 b). Then, instead of just two current density peaks occurring at E_c (Figure 2.7), in total four peaks are present in the loop as seen in Figure 2.10 b. The four peaks are related to the critical fields, E_f and E_a both in the positive and negative part of the field. The current density at E_f will be positive at positive field and negative at negative field, while it is opposite at E_a . Figure 2.10 c also shows a typical bipolar S-E curve for an antiferroelectric [14]. The large strain and hysteresis occur when the net polarisation is induced.

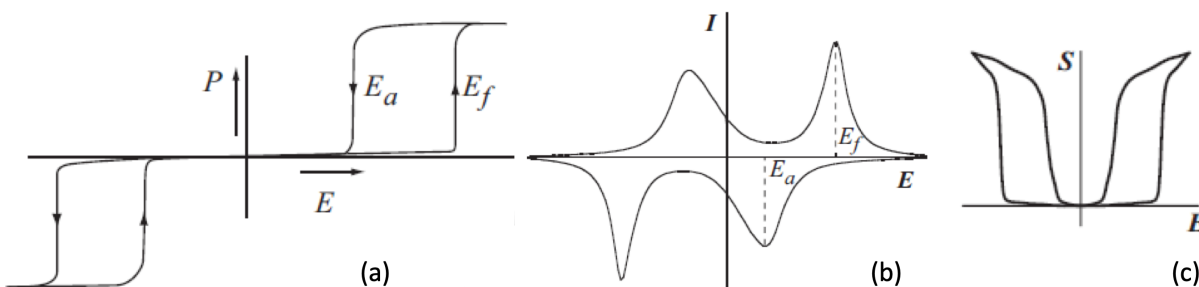


Figure 2.10: Double hysteresis. (a) P-E loop with trace of a field induced antiferroic-ferroic transition, which is reversible, in a P-E loop. (b) I-E loop with trace of a field induced antiferroic-ferroic transition, which is reversible. (c) S-E loop with trace of a field induced transition. Subfigures retrieved from [14, 17].

S-E curves can also reveal information about orientation or texturing of a sample. In most polycrystalline ferroelectrics the properties are mainly the same in all directions as a result of random orientation of grains [14, 18]. While in single crystal and textured ferroelectrics it is observed that their properties are strongly affected by which crystallographic direction measurements are carried out in. Further the positive or negative strain of a certain orientation direction can be higher or lower than another direction, thus the S-E curve can shift from being symmetrical positioned on the strain axis, to either more positive or more negative values. Figure 2.11 shows how the strain shifts, depending on in which direction the field is applied, on a PM N-0.29PT crystal.

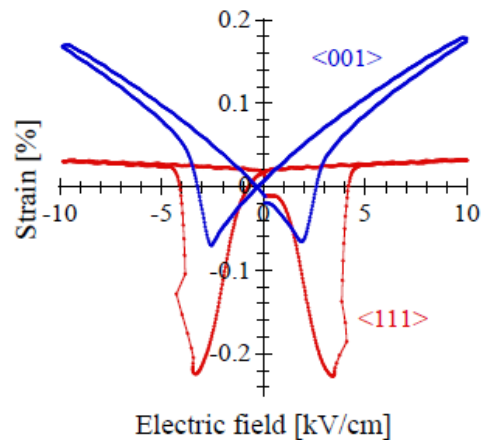


Figure 2.11: Orientation dependent strain behaviour of PM N-0.29PT. S-E curves for PM N-0.29PT crystal where the field is applied in the [011] direction (blue curve) and the [111] direction (red curve) Retrieved from [14].

2.2 Fracture surfaces and grain size determination

One can see illustrations of transgranular fracture in Figure 2.12 a and intergranular fracture in Figure 2.12 b. Intergranular fracture can be described as the fracture happening along the grain boundaries, while transgranular fracture happen through the bulk of the grain. Example of fracture surfaces with transgranular fracture can be seen in Figure 2.13 a and intergranular fracture can be observed in Figure 2.13 b.

A conventional way to determine the grain size of a polycrystalline material is to use an intercept method, such as described next. Straight lines of the same length is drawn through a variation of micrographs that show a polished fracture surface of the material of interest. All grains that intersect such a line segment are counted, and the length of one line segment is divided by the average number of grains intersecting such a line. Finally the average grain diameter is estimated by dividing this result by the linear magnification of the micrographs.

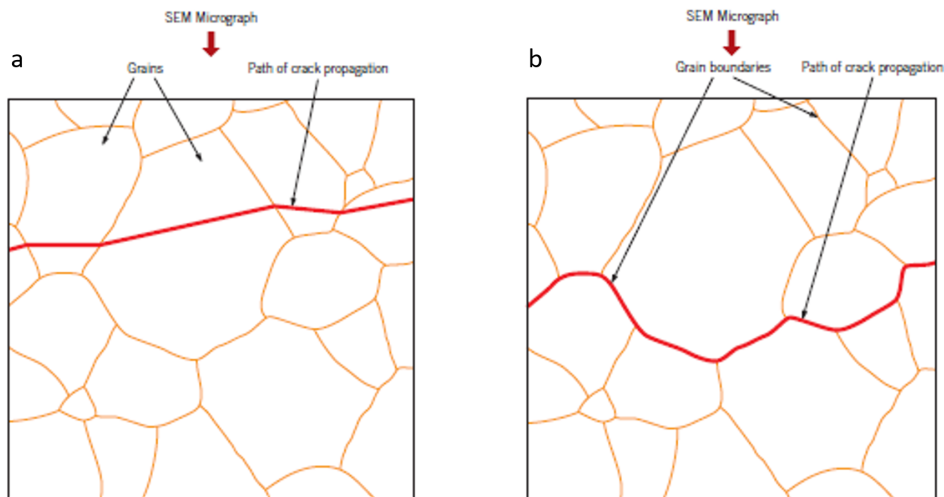


Figure 2.12: Illustration of transgranular (a) and intergranular (b) fracture. Transgranular fracture happens through the bulk of the grain, while intergranular fracture happens along the grain boundaries. Retrieved from [19].

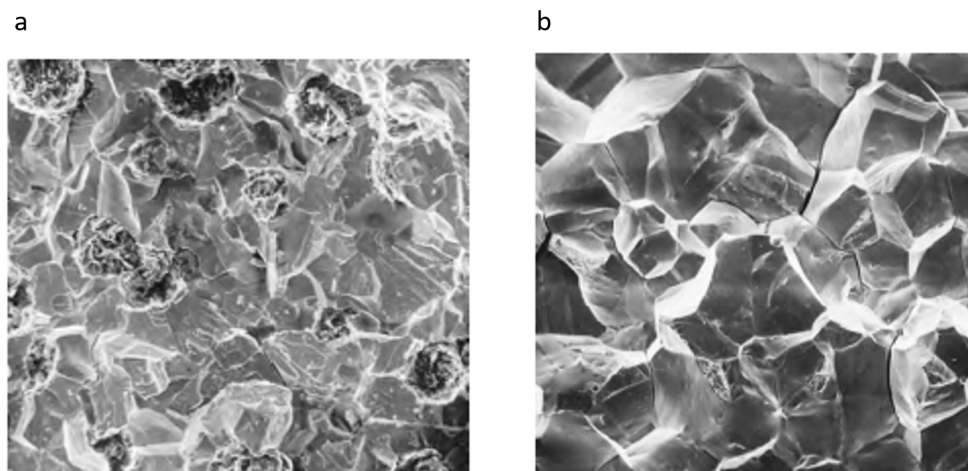


Figure 2.13: Micrographs of transgranular (a) and intergranular (b) fracture surfaces. Retrieved from [19].

2.3 Plastic Crystals

Plastic crystals were recognised and given its name by Timmermanns [20] in 1935. These materials have a cubic mesophase, also known as plastic crystal phase, that possess properties in between those of liquids and solid crystals. In an ordered crystalline solid the components will be fixed within a crystalline lattice, while molecules are free to move around and rotate freely as components of a liquid (Figure 2.14). The plastic crystal mesophase will have long range order, similar to the ordered solid crystals, as the mass centres of the molecules are fixed in a crystalline lattice. However, the molecules are free to rotate about the mass centre in the lattice, giving local disorder, such as for liquids [4, 21]. Because molecular rotations are activated before melting occurs, the entropy upon melting is lower for these materials compared to other organic crystals, and this is what raised Timmermanns interest for them in the first place. The plastic crystal phase is typi-

cally reached through one single or multiple solid-solid phase transitions where one can observe the component of rotation of the transition entropy [4, 22].

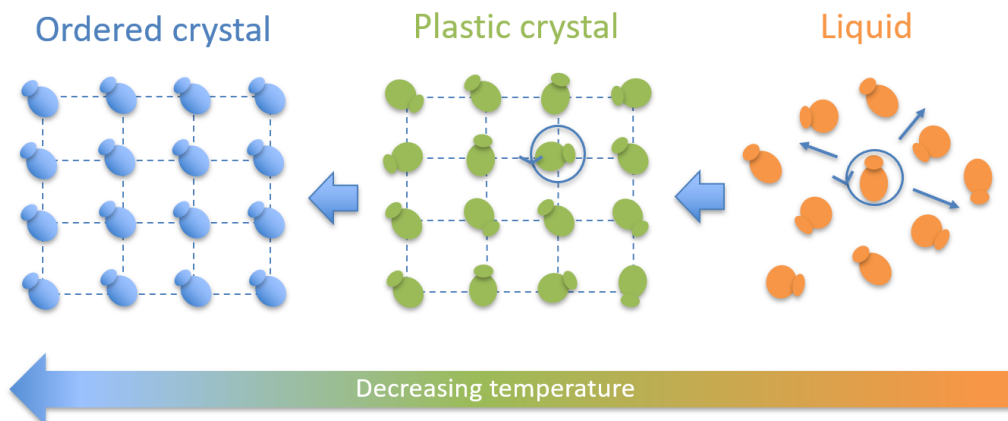


Figure 2.14: Plastic crystals phases are mesophases and they possess properties in between those of liquid, with molecular rotational freedom, and ordered solid crystals, with molecules fixed at certain crystal lattice sites. This gives long range order as in a solid, but also local disorder as in a liquid. Retrieved from [1]

The components in the plastic crystals phase will take up close to spherical space as they rotate, making dense cubic packing possible. This commonly leads the material to take on cubic symmetry, which is known to facilitate slip through numerous slip systems. The globular molecules of the plastic crystal phase will occupy a larger space than predicted in the crystalline phase, leading to weaker and more isotropic intermolecular interaction and thus also less energy being required to break bonds and initiate slip in the mesophase [23]. Therefore the plastic crystal phase is highly plastic. Plastic crystals that have constituents that are molecular cations and anions are called ionic plastic crystals. If only one of the molecular ions have rotational freedom, the entropy upon melting can be higher than observed for plastic crystals where all components are free to rotate in the mesophase [22].

2.3.1 Ferroelectric plastic crystals

The temperature at which a material transition from being polar, with ferroelectric properties, into being a non-polar paraelectric material is known as Curie temperature, T_C [15]. Some ionic plastic crystals show ferroelectric behaviour in some of their solid states. This is typically induced by rotation of their polar molecules [24]. Below the Curie temperature these will typically be pinned in specific positions. Cooling of globular ionic compounds leads the material to go through a number of solid-solid transitions where lower symmetry crystal phases are obtained and leaves the polar molecules with a certain degree of orientation. If this orientation can be switched by applying an electrical field, the material is a ferroelectric plastic crystal. On the contrary, when the temperature of such material is raised above its Curie temperature, disordering of the the polar groups will occur. Then the material will be centrosymmetric and not hold ferroelectric properties anymore.

2.4 Tetramethylammonium bromotrichloroferrate(III)

2.4.1 Structure and crystallographic phases

TMAFeBrCl₃ is a molecular organic ionic plastic crystal that has been studied by Harada *et. al.* [23] and Walker *et. al.* [25, 26] as a prototypical plastic crystal ferroelectric. The compound consists of the globular organic cation tetramethylammonium: [(CH₃)₄N]⁺ (TMA) and the tetragonal complex inorganic anion bromotrichloroferrate(III): [FeBrCl₃]⁻ (FeBrCl₃) (Figure 2.15). TMA is the most basic quaternary ammonium based cation, with nitrogen placed in the centre while four methyl (CH₃) groups surround it [27]. The TMA cations readily make salts with halides. Their globular nature in the compound with FeBrCl₃ is caused by their freedom to rotate [23]. In total four solid-solid phase transition, giving five distinct crystalline phases, have been reported for this particular and isostructural compounds [23, 25, 28]. These are labelled from I to V, where phase I is stable at the highest temperature, as by convention.

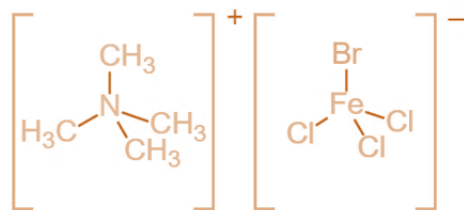


Figure 2.15: The molecular ionic compound TMAFeBrCl₃ consists of globular organic cations ([(CH₃)₄N]⁺) and tetragonal complex inorganic anions ([FeBrCl₃]⁻) [23].

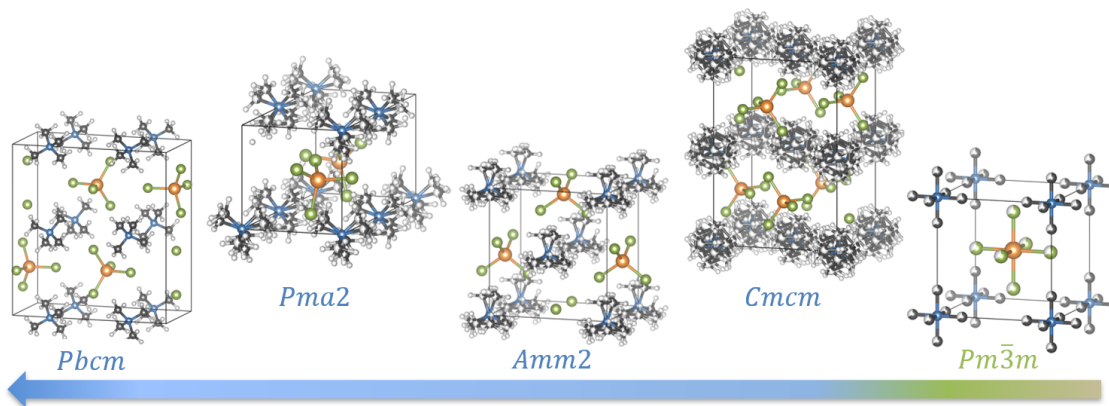


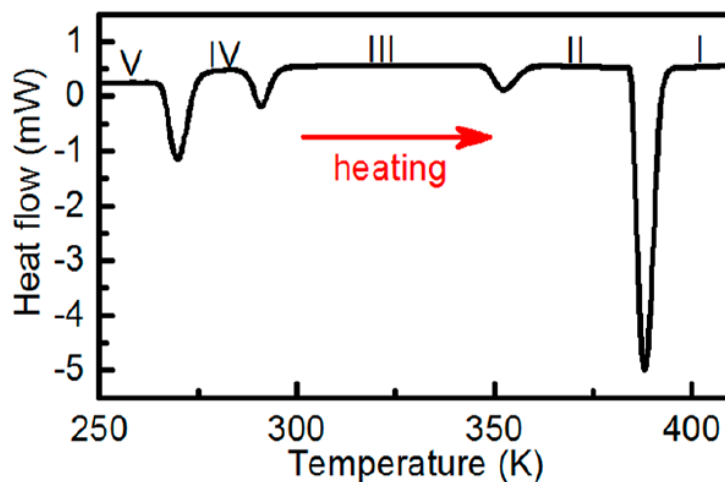
Figure 2.16: The five crystalline phases of TMAFeBrCl₃. They are labelled with the space group they belong to. Retrieved from [1].

Phase I of TMAFeBrCl₃ is stable at temperatures above 110 °C [23]. Then the compound crystallises in the CsCl-structure, which is a cubic Pm $\bar{3}$ m space group. This is the material's plastic crystal mesophase. By lowering the temperature the material will first transition into the orthorhombic Cmcm (II) structure at about 80 °C. Both Pm $\bar{3}$ m and Cmcm are centrosymmetric space groups. By further lowering the temperature to about 30 °C the second transition will leave the compound in the orthorhombic Amm2 (III) phase, which is non-centrosymmetric and thus ferroelectric. The next transition is into the orthorhombic Pma2 (IV), also being non-centrosymmetric and ferroelectric, at close to -10 °C. Finally, the lowest temperature phase stabilises below -25 °C

Table 2.1: Crystal data for TMAFeBrCl_3 retrieved from [23]

| Phase | Transition onset temperature | Crystal system | Space Group |
|-------|------------------------------|----------------|----------------------------|
| I | 384 K | cubic | $\text{Pm}\bar{3}\text{m}$ |
| II | 364 K | orthorombic | Cmcm |
| III | 285 K | orthorombic | $\text{Amm}2$ |
| IV | 263 K | orthorombic | $\text{Pma}2$ |
| V | >263K | orthorombic | Pbcm |

as orthorombic and centrosymmetric Pbcm space group. In Figure 2.17 one can see a DSC trace of the isostructural compound tetramethylammonium tetrachloroferrate(III): $[(\text{CH}_3)_4\text{N}]^+[\text{FeCl}_4]^-$ (TMAFeCl_3), obtained from [23]. The five crystalline phases structures are illustrated in Figure 2.16, which shows that it is only the globular cation TMA that has several orientations possible in phase II-IV, while in phase I both the cation and anion have many available orientations [23]. In the $\text{Pm}\bar{3}\text{m}$ phase both the cations and anions are shown as symmetric molecules as a representation of their rotational freedom yielding symmetry. In Table 2.1 one can find a summary of the space groups and which crystal systems the five phases belong to.

**Figure 2.17:** DSC trace of TMAFeBrCl_3 . Four phase transitions are observed if heating the material and the five crystalline phases are labelled as I-V where I is present at highest temperature. Retrieved from [23].

2.4.2 Synthesis and processing

Harada *et al.* report in [23] that they have been able to synthesise an orange powder of $[(\text{CH}_3)_4\text{N}][\text{FeBrCl}_3]$ by mixing equimolar amounts of tetramethylammonium bromide and iron(III)chloride hexahydrate in neutral water, removing the water and then purifying by recrystallisation from ethanol. Walker *et al.* [25, 26, 29] have reported various synthesis routes, where the main difference are the number of purifying recrystallisation steps. Both Harada *et al.* and Walker *et al.* achieved thin polycrystalline samples by plastically deform the material by pressing a crushed crystal powder. In [25] the preferred orientation in the pressed samples is observed from XRD. Our previous work [1] shows that phase stability of TMAFeBrCl_3 is susceptible to changes in synthesis and processing. Namely, the phase stability of the above room temperature phase Cmcm down to 25 °C.

2.4.3 Vibrational spectroscopy

From previous Raman studies on TMAFeBrCl_3 and similar compounds it is expected that the complex inorganic anion bands are located at low wavenumbers, while contribution from the organic cation bands are located at above 400 cm^{-1} [25, 30–33]. IR spectroscopy of the material has only shown contribution from the organic cation. The molecular group TMA has tetrahedral (T_d) symmetry in its free state [31, 33]. The internal vibrations of TMA can be divided into CH_3 group vibrations and skeletal vibrations of C_4N . The TMA ion gives in total 45 internal modes of vibration, which of 19 are fundamental vibrations. The inorganic cation, also hold tetragonal symmetry and vibrational modes of the Fe-Br and Fe-Cl bands, as well vibrations associated with the ion itself is expected [25, 30].

Temperature dependent raman studies on layered CuCl_4 -based organic-inorganic hybrid has been carried out by Caretta et al. [34]. The study shows that phase transition can be signed by broadening and decrease of band intensity as the system goes through symmetry changes when increasing the temperature (Figure 2.18).

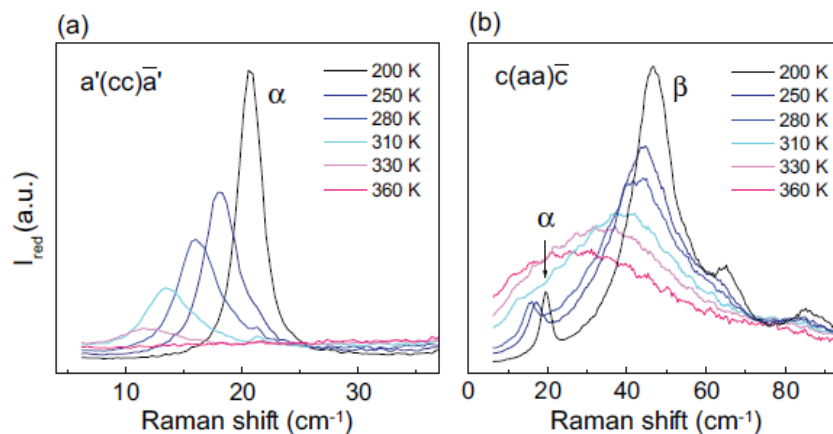


Figure 2.18: Broadening and softening observed in low frequency α (a) and β (b) phonons of layered CuCl_4 -based organic-inorganic hybrid upon increasing temperature. On heating, the modes continuously soften and broaden. Retrieved from [34].

2.4.4 Electrical properties

Harada et al. [23] report that the P-E hysteresis behaviour of TMAFeBrCl_3 shows minimum field strength to achieve polarisation inversion at 67 kV/cm , which is quite small yield P_r of $4.5 \mu\text{C/cm}^2$. Walker et al. [25, 26] have studied the P-E, I-E and S-E hysteresis behaviour of the material, which have yielded various results. In [25] the study was carried out by increasing the electrical field from 20-80 kV/cm at 10 Hz. 80 kV/cm was chosen as maximum due to dielectric breakdown at higher fields. The P-E loops showed progressive development into square like hysteresis which is characteristic for ferroelectric materials, however rounding of the loop corners reveal that leakage current was present. Apparent remnant polarisation, P_r^* is reported to rise from 1.2-2.9 $\mu\text{C/cm}^2$ between 60-80 kV/cm , which is suggested to be partly caused by the leakage current. The S-E loops also went through a progressive opening from small butterfly-like loops to having a peak-to-peak strain (S_{PP}) of 0.019% at 60 kV/cm and 0.048% at 80 kV/cm . In [26] Walker et al. cycle their pressed TMAFeBrCl_3 samples all the way up to 260 kV/cm . The P_r^* showed linear growth up

to 170 kV/cm and values of $5 \mu\text{C}/\text{cm}^2$ at 150 kV/cm and $10 \mu\text{C}/\text{cm}^2$ at 260 kV/cm is reported, sharp current density peaks in the I-E loops indicated ease of domain switching within the material, while the S_{PP} increased from 0.014% to 0.109% between field amplitudes of 80 and 170 kV/cm, after which it plateaued. In [26] the P-E, I-E and S-E behaviour was also studied as a function of frequency, where reversible asymmetric switching behaviour is observed at high frequency. This is suggested to be facilitated by an internal field bias, which is related to incomplete reversal of the domains upon switching, which again is caused by time dependency and would be largely promoted by defects present in the material [25].

3 Experimental

3.1 Synthesis of tetramethylammonium bromotrichlorideferrate(III) crystals by slow evaporation from water

Synthesis (see schematic in Figure 3.1) was carried out starting with the precursors tetramethylammonium bromide: $(\text{CH}_3)_4\text{NBr}$ (TMABr) and iron(III)chloride $\text{FeCl}_3 \cdot 6\text{H}_2\text{O}$. The precursors TMABr (7.2559 g) and iron(III)chloride hexahydrate (12.7412 g) were weighed out (METTLER TOLEDO, 3.2) to achieve a 1:1 stoichiometric ratio and then dissolved in 20 mL deionised water each. The two precursor solutions were mixed and stirred for approximately 15 minutes with a magnetic stirrer (IKA RTC Classic). The solution was kept in a ventilated area in a Petri dish covered with a layer of pin-holed aluminium foil for 16 days until the water had evaporated. When a crystal layer covered the entire Petri dish, it was broken up to make sure as much water as possible could evaporate. The crystal agglomerates formed by this synthesis will be denoted as C-Agl (Table 3.1).

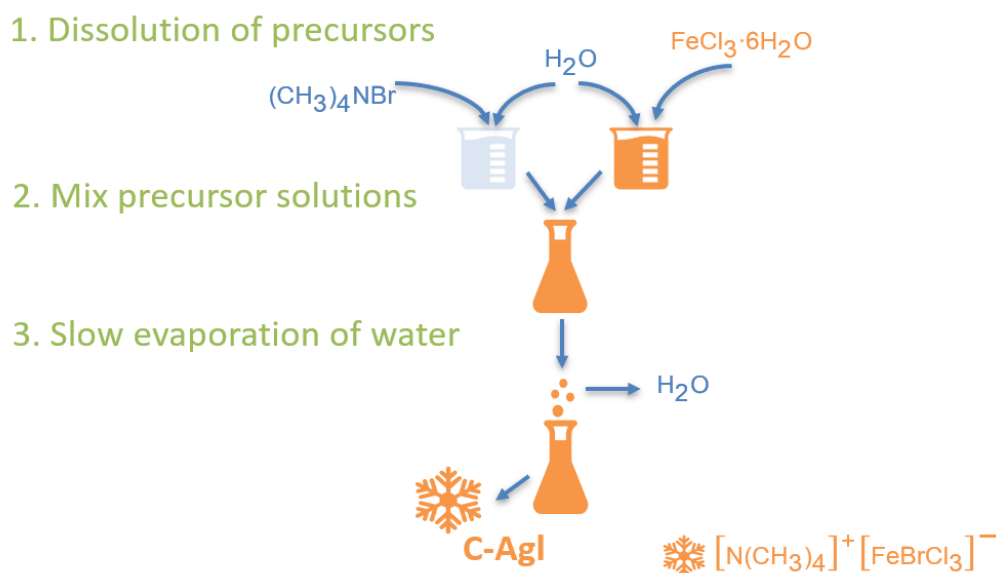


Figure 3.1: Synthesis route: First, the two precursors $(\text{CH}_3)_4\text{NBr}$ and $\text{FeCl}_3 \cdot 6\text{H}_2\text{O}$ are separately dissolved (1) in deionised water, before the solutions are mixed (2). The water of the solution is removed by slow evaporation (3) that eventually result in formation of TMAFeBrCl₃ crystal agglomerates; C-Agl.

Before any characterisation or further processing was done, the crystals (C-Agl) were dried in a vacuum drying furnace (Binder VD23). The sample was dried at 50 °C overnight (14 hours). The sample was left to cool. Some crystal agglomerates were crushed down to the two powder samples C-Pow-1 and C-Pow-2. C-Pow-1 crystals were dried in the same manner for 2 hours at 50 °C.

3.2 Pressing of polycrystalline samples

In total eight samples were prepared by hot-pressing (Figure 3.2). Four of the samples were pressed directly from crystal agglomerates (C-Agl) of approximate weight of 0.2 g. The pressed agglomerates will be denoted by P-Agl-1, P-Agl-2, P-Agl-3 and P-Agl-4. The remaining four pressed samples were prepared by pressing the crushed powders into disk samples denoted as P-Pow-1, P-Pow-2, P-Pow-3 and P-Pow-4. P-Pow-1 was pressed from C-Pow-1, while the rest was pressed from

Table 3.1: Crystals and pressed samples produced

| Sample name | Description | Weight | Characterisation |
|-------------|--------------------------------|--------|------------------------------|
| C-Agl | From slow evaporation of water | - | - |
| C-Pow-1 | Powder crushed from C-Agl | - | XRD |
| C-Pow-2 | Powder crushed from C-Agl | - | XRD |
| P-Agl-1 | Pressed from C-Agl | 0.23 g | XRD,SEM,Raman,FTIR, El.meas. |
| P-Agl-2 | Pressed from C-Agl | 0.27 g | XRD,SEM,DSC,FTIR, El.meas. |
| P-Agl-3 | Pressed from C-Agl | 0.26 g | XRD |
| P-Agl-4 | Pressed from C-Agl | 0.16 g | XRD,DSC, El.meas. |
| P-Pow-1 | Pressed from C-Pow-1 | 0.22 g | XRD,SEM,FTIR,El.meas. |
| P-Pow-2 | Pressed from C-Pow-2 | 0.21 g | XRD,DSC,FTIR, El.meas. |
| P-Pow-3 | Pressed from C-Pow-2 | 0.20 g | XRD,SEM,DSC |
| P-Pow-4 | Pressed from C-Pow-2 | 0.20 g | XRD |

C-Pow-2. The C-Pow-1 sample was also dried again before being pressed. Approximately 0.2 g of C-Pow was used for each P-Pow sample. When pressing both powder and agglomerates, the crystals were placed in the middle of a square steel plate (5x5 cm²) covered with Teflon foil before another Teflon foil-covered steel plate was then placed face down on top of the sample. The steel-plate-crystal-sandwich was put into a hot press (Carver) in which both the top and bottom plates were preheated to 125 °C. The samples were preheated by closing the hot press, so that it applied a light pressure, before further closing until approximately 3.9 MPa was applied. This pressure was maintained for 15 minutes and then released. As the samples were not laterally contained, when pressing C-Pow, some powder at disc edges did not densify and was thus removed from the sample with tweezers.

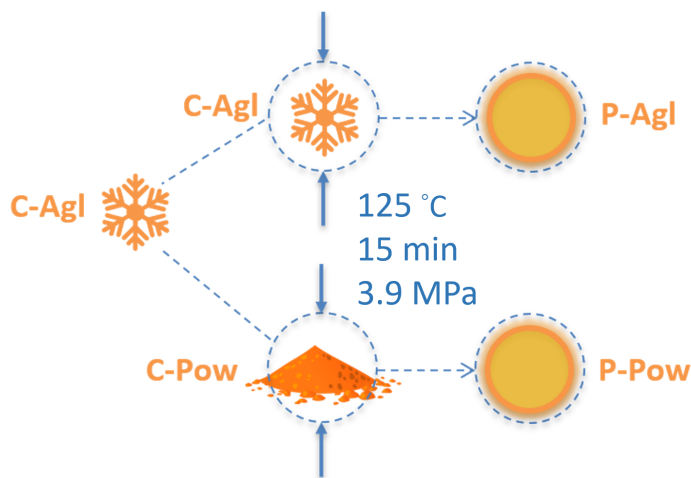


Figure 3.2: Hot-pressing: Crystal agglomerates (C-Agl) of TMAFeBrCl₃ were either hot pressed directly (P-Agl) or crushed down to a powder (C-Pow) and then pressed (P-Pow) into thin disk shaped polycrystalline samples. The pressing was done at 125 °C with approximately 3.9 MPa applied for 15 minutes.

3.3 Characterisation

3.3.1 Crystal microstructure

To look closer at the microstructure of the samples scanning electron microscope (SEM) imaging (Hitachi S3400N) of fracture surfaces of P-Agl-1, P-Agl-2, P-Pow-1 and P-Pow-3 was carried out (Table 3.1). The fracture surface was prepared by bending part of the thin sample with tweezers, until it fractured. The smallest piece of sample to be fractured was fastened with carbon tape to a cylindrical sample stub with a middle wall, such that the fracture surfaces were facing up.

3.3.2 Crystallographic structures

XRD analysis was performed on two powder samples, C-Pow-1 and C-Pow-2 as well as the eight pressed samples, all mentioned in Table 3.1. The two equal powdered samples C-Pow-1 and C-Pow-2 were prepared by using a mortar to crush crystal agglomerates, C-Agl, prepared by the synthesis described in 3.1, down to a fine powder. Specific preparation before XRD analysis included placing the fine powder in the cavity of a standard XRD sample holder, before swiping a glass slide along the edge of the holder to level the powder with the holder to create a flat and continuous surface. All pressed samples were placed in deep-cavity sample holders and were fastened to and kept level with the holders. All XRD measurements were performed on a Bruker D8 A25 DaVinci X-ray diffractometer with $\text{CuK}\alpha$ radiation ($\hbar\omega = 8.04 \text{ keV}$, $\lambda = 1.5406 \text{ \AA}$). The characterisation was done from 10-75 degrees 2θ , for 120 minutes with 0.2° slit-opening for all samples except P-Pow-2, which was characterised from 5-75 degrees 2θ , for 120 minutes with 0.1° slit-opening.

Rietveld-refinement

The XRD data was fitted with the DIFFRAC.SUITE TOPAS[®] software. The Amm2 and Cmcm phase from Cambridge crystallographic data center (CCDC) file 1574204 and 1574206, respectively, produced from Harada *et. al.* [23], were used to perform the fit. When fitting gave inconclusive results, fitting towards the solid Pma2 phase, using appropriate CCDC file, were carried out. Two bromide (Br) ions were added to two of the chloride (Cl) ion sites in the structure, with an occupancy of 0.125. The occupancy of chlorine was thus reduced from 1 down to 0.875. The atomic positions were not refined. Upon the analysis, scaling, microstructure crystal L size, sample displacement and a third order background polynomial towards the Amm2 phase, was first refined. Then, the lattice parameters were opened for Amm2, before the Cmcm phase was included to the refinement. The scale and lattice parameters were both opened for refinement when the Cmcm phase was included. The background polynomial order was increased to four if this could improve the fit. Finally a preferred orientation with a spherical harmonics function of fourth order for both Amm2 and Cmcm phase was used.

3.3.3 Vibrational spectroscopy

Raman spectroscopy

An in situ temperature dependent Raman spectroscopy study was done on the P-Agl-1 sample (Table 3.1). The study was performed with the WITec alpha300 R confocal Raman spectrometer, with a 532 nm laser. Calibration of the instrument was done using a single crystal silicon sample. The temperature dependent study was enabled by using a Harrick Raman High Temperature Reaction Chamber, and temperature adjustment was facilitated by a Harrick temperature controller, that was manually controlled, and water cooling.

Before the measurements the sample was cut to a size such that it could fit on top of a wire mesh of 6.3 mm diameter, that is placed in the reaction chamber. The thermocouple monitoring the temperature in the reaction chamber was located just under the mesh. The chamber was closed with a SiO₂ window, and placed under a 10X lens of the spectrometer. Up to ten single spectra were collected at various points at each of the three temperatures, 30, 80 and 125 °C. Each single spectrum acquisition was done with a laser power of 0.3 mW in one accumulation with integration time of either 120 or 180 seconds. A 600g/mm grating was used and the spectral centre was at 2200 cm⁻¹.

Each spectrum was evaluated with respect to cosmic rays, and the WITec Project Fives Software cosmic ray removal (CRR) algorithm was applied with varying dynamic factor, which is the algorithms sensitivity to cosmic rays, to remove cosmic rays. When cosmic rays were removed, each spectrum was normalised. Then all the spectra collected at one specific temperature were used to calculate and plot average spectra at each of the three temperatures. For spectra which the software algorithm did not give satisfactory result, the specific spectrum was taken out of the specific range it affected.

For some specific bands in the averaged spectra of the Raman temperature series, band fitting and full width at half maximum (FWHM) calculation was done. Before performing a fit a constant local baseline value, corresponding to the relevant bands wavenumber range, was subtracted from the data. The fit was done using MATLAB curve fitting toolbox TM by applying a number of Gaussian curves. The FWHM value was then achieved by finding where a horizontal line at the half point between the baseline (zero) and maximum intensity of the fitted curve, intersected the same fitted curve.

Attenuated total reflectance Fourier transform infrared spectroscopy To compliment the Raman study attenuated total reflectance (ATR)-Fourier transformation infrared (FTIR) was carried out on the following samples; P-Agl-1, P-Agl-2, P-Pow-1 and P-Pow-2 (Table 3.1). 100 scans were done for all samples, and in addition a run of 250 scans were also recorded on the sample P-Agl-1. The sampling was recorded in the range 350-4000 cm⁻¹ by a Bruker Vertex 80v FTIR spectrometer with a diamond crystal. The samples are placed in direct contact with the crystal and the beam of infrared light travel through the diamond crystal into the sample, as an evanescent wave, giving depth of penetration of typically 0.5-2 μm.

3.3.4 Phase transitions

DSC measurements were carried out on the following samples: C-Pow-2, P-Agl-2, P-Agl-2, P-Pow-2 and P-Pow-3 (Table 3.1). About 5-10 mg of each sample was placed in a aluminium crucible each which were closed off by a lid and pressed on with a pressing tool. Each crucible, with lid, was weighted before and after adding the plastic crystal sample. The reference weight of the crucible and lid were entered to the instrument software of Netzsch DSC 214 Polyma. Then each of the samples was placed in the instrument, starting with an empty reference crucible. First two consecutive heating cycles were run on all the samples. The heating/cooling rate was set to 10 °C per minute between -25 and 200 °C, with a hold time of 10 minutes at maximum temperature. A mix of synthetic air and nitrogen, with a flow rate of 50 mL/min, was used to provide gas flow and to function as a protective gas, respectively. Purge was not used. Additionally, a second set of four cycles was run on the C-Pow-2, P-Agl-2 and P-Pow-2 samples.

3.3.5 Electrical properties

Electrical measurements were carried out on the pressed samples P-Agl-1, P-Agl-2, P-Agl-4, P-Pow-1 and P-Pow-2 (Table 3.2). First the pressed samples were made ready for electrical measurements by cutting them into pieces of approximately 10 mm² and depositing 3 mm diameter gold electrodes on both sides using a shadow mask. Both current-voltage and hysteresis measurements were done using an Aixacct ferroelectric tester, a Trek 10 kV signal amplifier and a laser interferometer for strain measurements.

Current-voltage measurements, in 1 kV/cm steps between -10 and +10 kV/cm on both increasing and decreasing field, were performed on the four samples P-Agl-1, P-Agl-2, P-Agl-4 and P-Pow-2. For sample P-Pow-1 the current-voltage measurement was done similarly, but in 1 kV/cm steps between -20 and +20 kV/cm. Current data was recorded at each step after 10 seconds.

For all hysteresis measurements a triangular waveform was used. For the samples P-Agl-1, P-Agl-2, P-Agl-4 and P-Pow-2 the electrical field was initially increased in intervals of 10 kV/cm from zero to 200 kV/cm at 10Hz. Then a frequency sweep where hysteresis measurements with electrical field of 200 kV/cm was measured at various frequencies going from 100 to 1Hz. Finally the electrical field was again increased in intervals of 10 kV/cm up to maximum field at 10 Hz, except for sample P-Agl-1 where 200 kV/cm was the maximum field. For sample P-Pow-1 the electrical field was driven to 400 kV/cm before the frequency sweep between 100 and 1 Hz was performed. An insulating Silicone oil was used to prevent arcing at high fields. Current-voltage measurements were again done after the hysteresis measurement cycling.

Table 3.2: Instruments used in this study

| Instrument | Model |
|-------------------------------------|---|
| Scales | Sartorius, METTLER TOLEDO Ag204 Delta Range |
| XRD | Bruker D8 A25 DaVinci |
| SEM | Hitachi S3400N |
| Hot-press | Carver |
| Magnetic stirrer/hot plate | IKA RTC Classic |
| vacuum drying furnace | Binder VD23 |
| DSC | Netzsch DSC 214 Polyma |
| Ferroelectric tester | Aixacct |
| Signal amplifier | Trek (10kV) |
| Raman confocal imaging spectrometer | alpha300 R |
| FTIR Spectrometer | Bruker Vertex 80v |

4 Results

4.1 Observation upon synthesis and pressing

Starting with two precursor solutions, mixing them to a final solution and letting the solvent, being water, slowly evaporate gave a batch of crystal agglomerates, as explained in the section 3.1. When the precursors were dissolved in deionised water, the TMABr-solution was clear, whereas the iron chloride solution took a dark brown colour from the iron ions present. The mixed solution also took the same dark brown colour, as can be seen in Figure 4.1 a. Upon dehydration through slow evaporation of the mixed solution, crystals agglomerates (C-Agl) were precipitated. Crystals gradually precipitated on the surface of the solution, as one can see in Figure 4.1 b-c, and this was cracked open in order for all the solvent to evaporate. As one can see in Figure 4.1 d, the resulting agglomerates were brown in colour, but also with a hint of orange tint in the thinner sections, such as the edges.

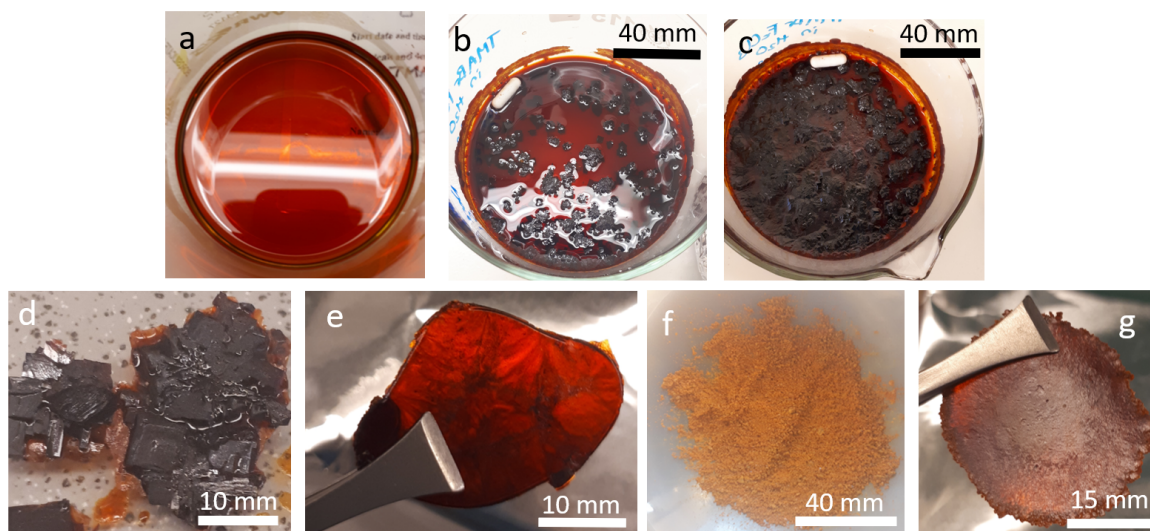


Figure 4.1: Slow evaporation synthesis and pressing of samples directly from crystal agglomerates and from powdered crystals. The scalebars are only approximate.

Figure 4.1 e shows a translucent red P-Agl sample with various 'shades' of lighter and darker colour. The bright orange powder resulting from crushing the agglomerates is shown in Figure 4.1 f. Pressing powder gave translucent orange sample, where finer powder grains can be seen on the surface (Figure 4.1 g). Images of all pressed samples are shown in Figure 4.2.

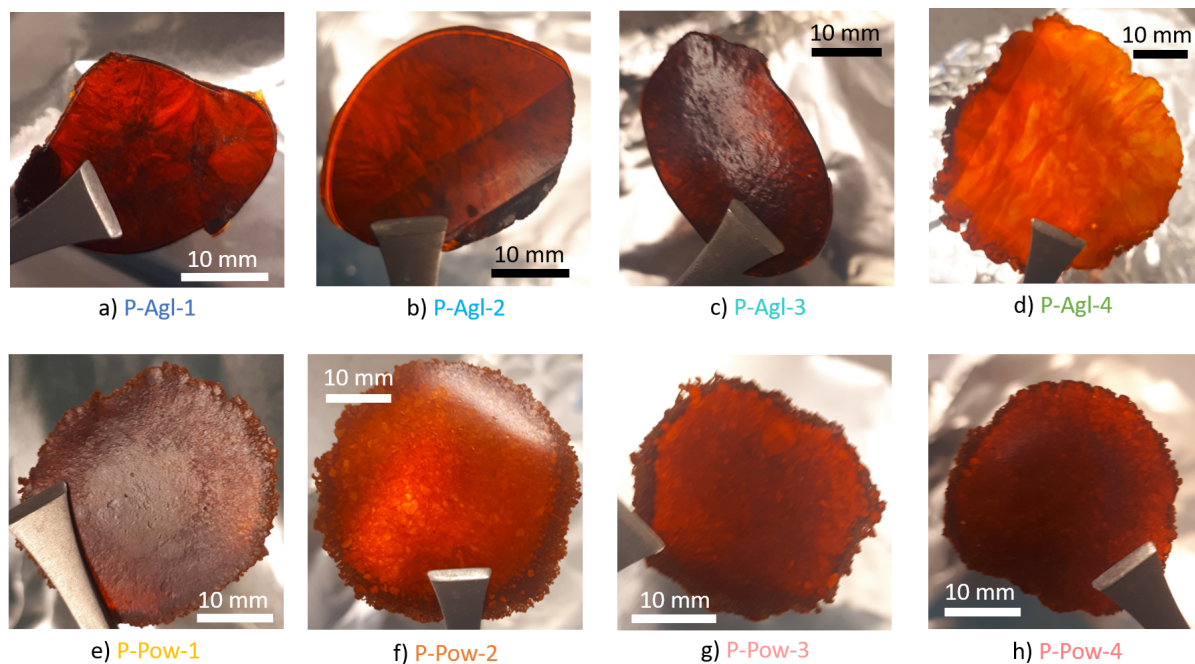


Figure 4.2: Slow evaporation synthesis and pressing of samples directly from crystal agglomerates and from powdered crystals. (a) Synthesis solution. (b) Crystals precipitating on the solution surface. (c) Precipitated crystal cover the solution surface. (d) Crystal agglomerates (C-Agl). (e) Pressed agglomerate sample (P-Agl). (f) Crushed agglomerate powder (C-Pow). (g) Pressed powder sample (P-Pow). Scalebars are only approximate.

4.2 Sample microstructures

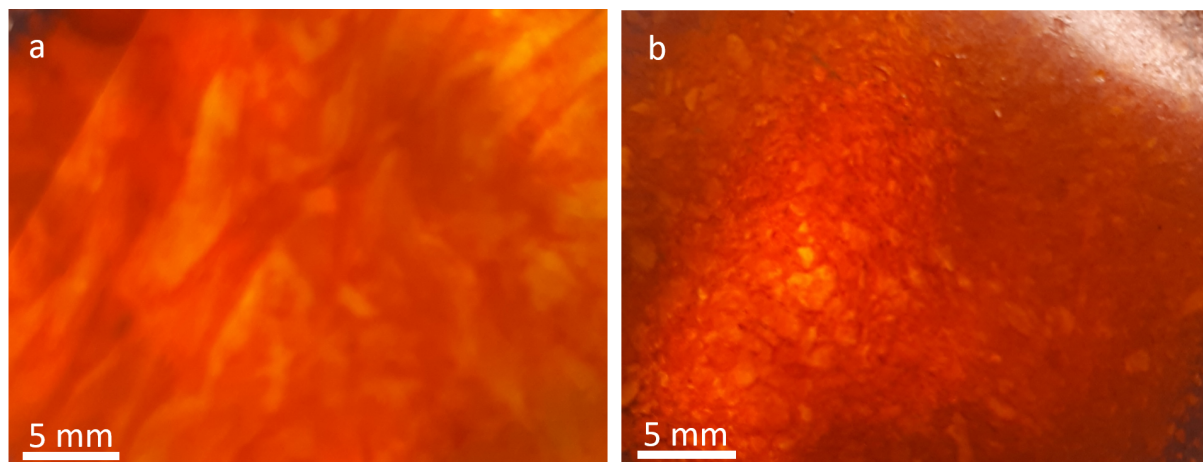


Figure 4.3: Images of the pressed samples P-Agl-4 and P-Pow-2 showing that the microstructure for pressed agglomerate and pressed powder is different. In the pressed powder sample (P-Pow-2), showed in b, one can observe smaller grains. The scale bars are only approximate.

The microstructure of the pressed crystal agglomerate sample P-Agl-4 and the pressed powder sample P-Pow-2 can be seen in Figure 4.3 a and b, respectively. In the pressed sample (P-Pow-2) the average grain size appears to be smaller than visible in the samples pressed from agglomerates.

Additionally, one can have a closer look at the two pressed samples P-Pow-1 and P-Pow-2 in Figure 4.4 a and b, pressed from the crushed agglomerate powders C-Pow-1 and C-Pow-2, respectively. The crystal size of sample P-Pow-1 appear to be smaller than for sample P-Pow-2.

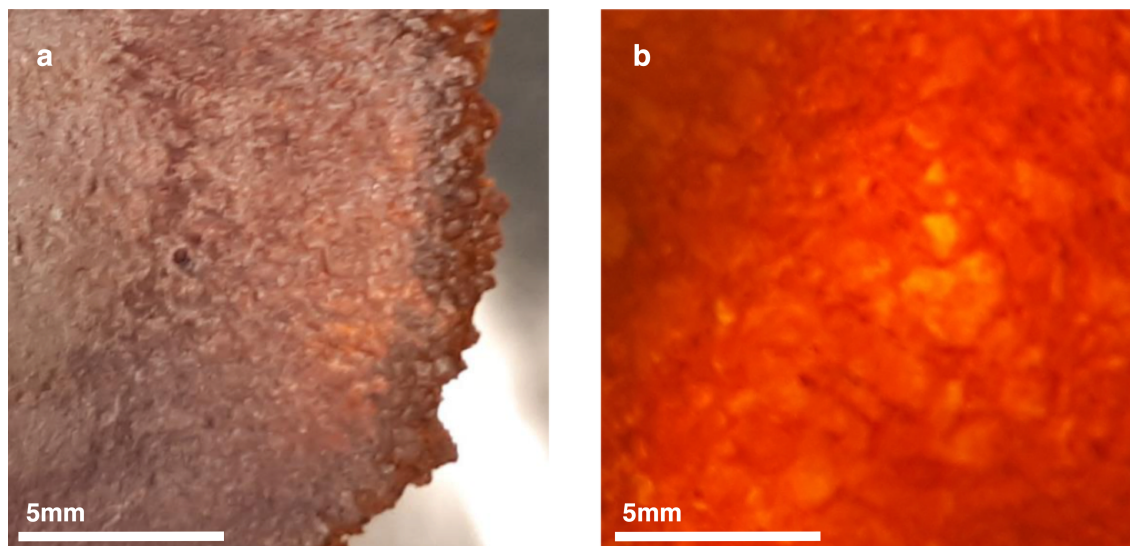


Figure 4.4: Images of the pressed samples P-Pow-1 (a) and P-Pow-2 (b) showing that the microstructure for pressed powder P-Pow-1 and P-Pow-2 samples, which is pressed from the two crushed powders C-Pow-1 and C-Pow-2, respectively, vary. The grain size of P-Pow-1 appear to be smallest. The scale bars are only approximate.

SEM imaging was performed in order to further investigate if it is possible to identify microstructural variation that can confirm the grain size differences, observed in the optical images, between pressed samples. Fracture surfaces of two pressed agglomerate samples, P-Agl-1 and P-Agl-2, and two pressed powder samples, P-Pow-2 and P-Pow-3, were studied and the key features visible in the fracture surfaces are detailed below.

The set of images in Figure 4.5 allows us to look at the variable microstructure of fracture surface cross section of sample P-Agl-1, at different magnifications. Figure 4.5 a_i shows the whole width of one part of the fracture surface cross section, while Figure 4.5 a_{ii} shows a higher magnification of the same area. One can see that both smooth and rough surface texture is present. The difference is better seen in Figure 4.5 $a_{iii}-a_v$, where the coloured squares have been further magnified to show the difference between the smooth and more textured rough surface. Another feature present at various points of the fracture surface is relatively large (100-300 μm) flat looking areas (yellow arrows) that can be observed in Figure 4.5 b and c. The surfaces of these flat areas seem to be sharp cut edges, but some scratch like lines are present (purple arrow). The scratches are going in various directions and could possibly be caused during sample preparation. Flat looking areas can also be observed in Figure 4.5 d. However, these areas differ somewhat from the flat areas seen in Figure 4.5 b and c, in terms of being smaller and being partly non-parallel to the fracture surface.

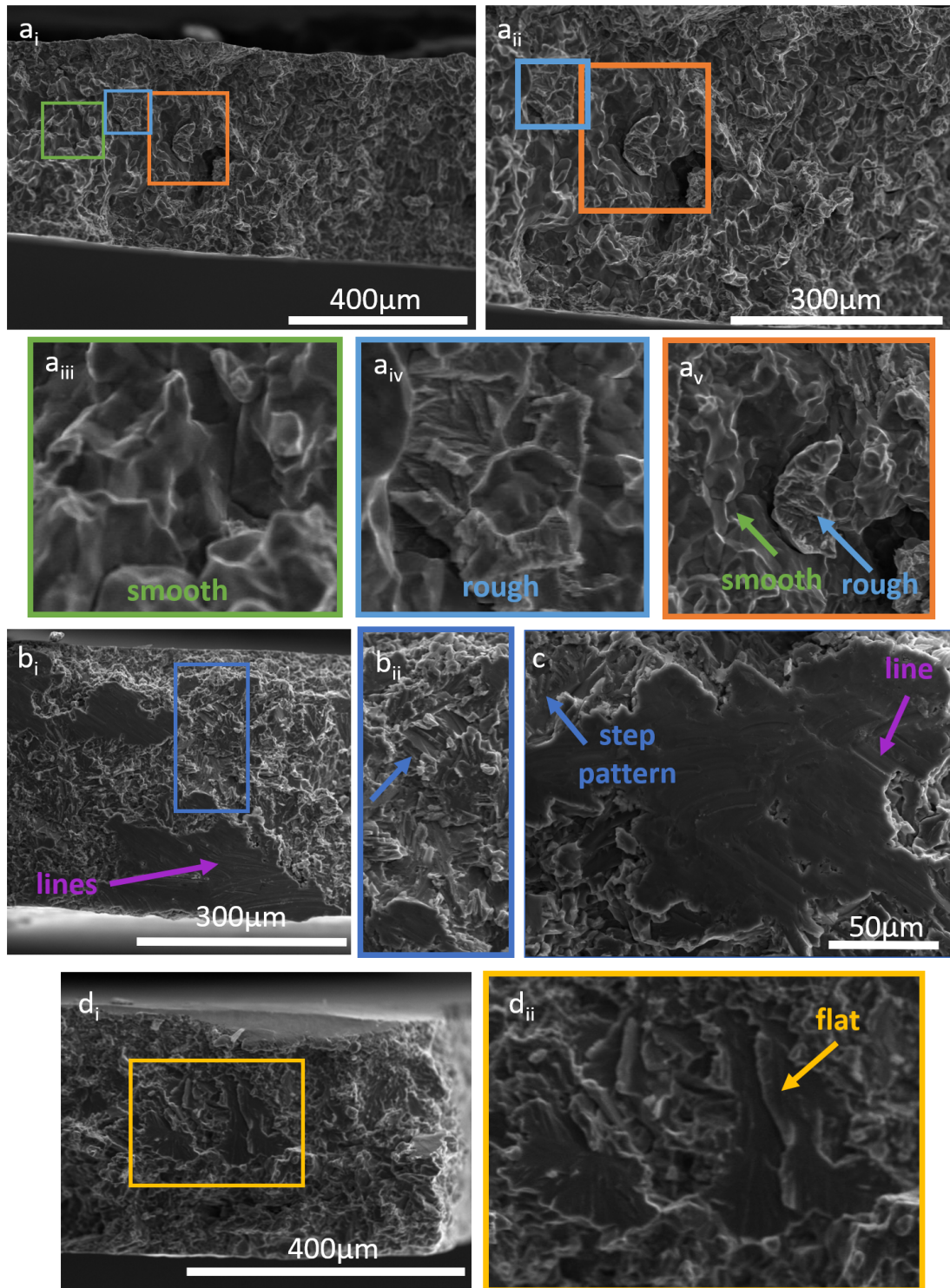


Figure 4.5: SEM images showing the microstructure of the pressed sample P-Agl-1. a_i shows a part of the fracture surface cross section, showing both smooth and more rough surface texture. a_i : Full width of fracture surface cross section. a_{ii} Closer look at fracture surface cross section. a_{iii} : Magnification of green square, showing smooth texture. a_{iv} Magnification of blue square, showing rough texture. a_v magnification of orange square, showing both smooth and rough texture. In b , c and d another part of the cross section show that also flat areas are present on the fracture surface. b_i : flat area surrounded by rough texture. d_i : Full width of cross section. d_{ii} Magnification of the yellow square, showing flat area that is parallel to fracture surface.

In Figure 4.6 the fracture surface cross section of the sample P-Agl-2 is shown. In Figure 4.6 a_i one can see full width of one part of the cross section and the surface texture seems to be mostly smooth, such as can be seen in Figure 4.6 a_{ii} , a magnification of the area within the green square in Figure 4.6 a_i . There are also some larger flat looking areas, such as seen in Figure 4.6 a_{iii} , magnification of the yellow square in Figure 4.6 a_i . In Figure 4.7 SEM images of a fracture surface in the P-Pow-1 sample are given. In Figure 4.7 a_i we see one of the edges of the sample cross section. At first glance this surface looks quite rough. However when looking closer at the magnification of the area within the orange square (Figure 4.8 a_{ii}) one can see that actually only a minor part of the surface have a rough texture (blue arrow) while the smooth looking areas (green arrow) make up much of the surface. There are also some flat looking areas, with width and height of approximately $100\ \mu\text{m}$, present (yellow arrow). In Figure 4.7 b a different part of the fracture surface, which has a different appearance than the edge seen in Figure 4.7 a, is given. Overall the surface has less distinct and smaller variation of features (Figure 4.7 b_i). The surface seem to generally be quite rough, however, with a close look one can observe that both jiggered rough areas such as seen in Figure 4.7 b_{ii} and smooth surfaces such as seen Figure 4.7 b_{iii} is present. The set of SEM images seen in Figure 4.8 show a fracture surface in the sample P-Pow-3. In Figure 4.8 a_i one can see the cross section of the edge of the fracture surface. Some flat looking areas can be observed in this sample. A closer look at two of such areas can be seen in Figure 4.8 a_{ii} and a_{iii} . The flat areas shown have width and height of about $100\ \mu\text{m}$. In Figure 4.8 b one can see the structure of the surface outside the flat looking areas shown in 4.6 a. The features are small and thus difficult to interpret in detail but when looking closer at Figure 4.8 b_i it looks like the features have rounded edges giving a relatively smooth fracture surface.

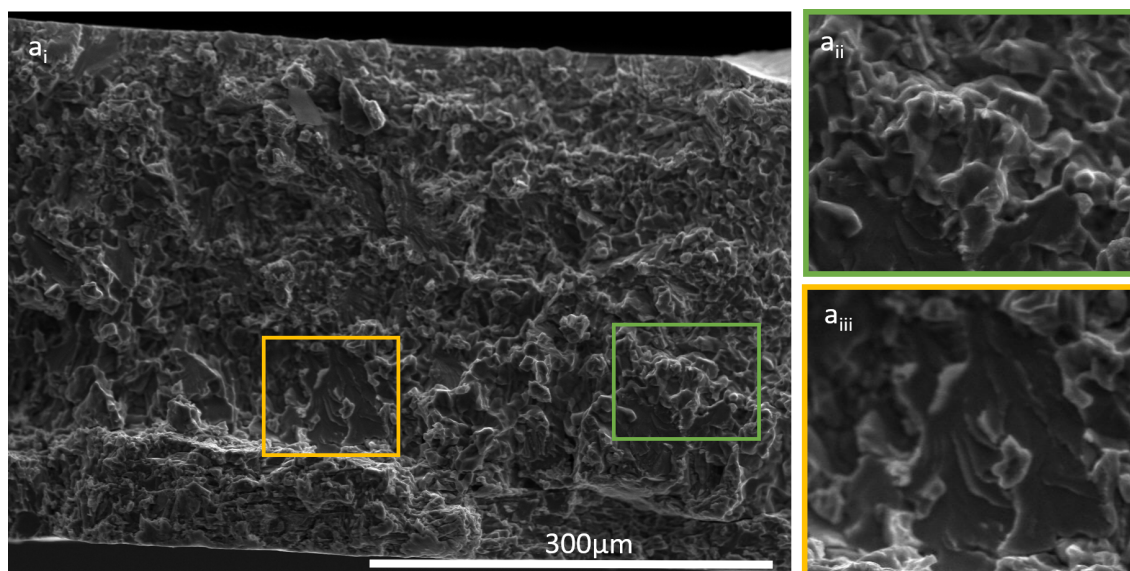


Figure 4.6: SEM images showing the microstructure of the pressed sample P-Agl-2. a_i : The full width of the fracture surface cross section, that look quite rough. a_{ii} : Magnification of the green square show the smooth texture that makes up the majority of the surface. a_{iii} : Magnification of the yellow square a flat looking area can be seen.

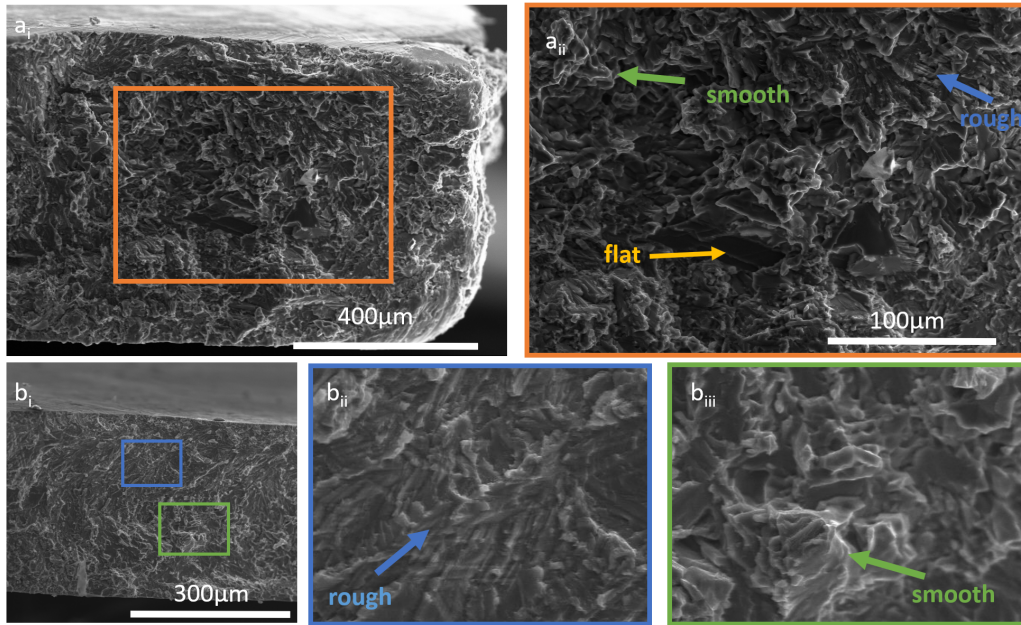


Figure 4.7: SEM images showing the microstructure of the pressed sample P-Pow-1. a_i : show the full width of the fracture surface cross section. a_{ii} : Magnification of the orange square show that smooth and rough texture, as well as flat areas are present. b_i : A different part of the cross section. b_{ii} : Magnification of the blue square showing a rough jiggered step like pattern. b_{iii} : Magnification of the green square showing smooth texture.

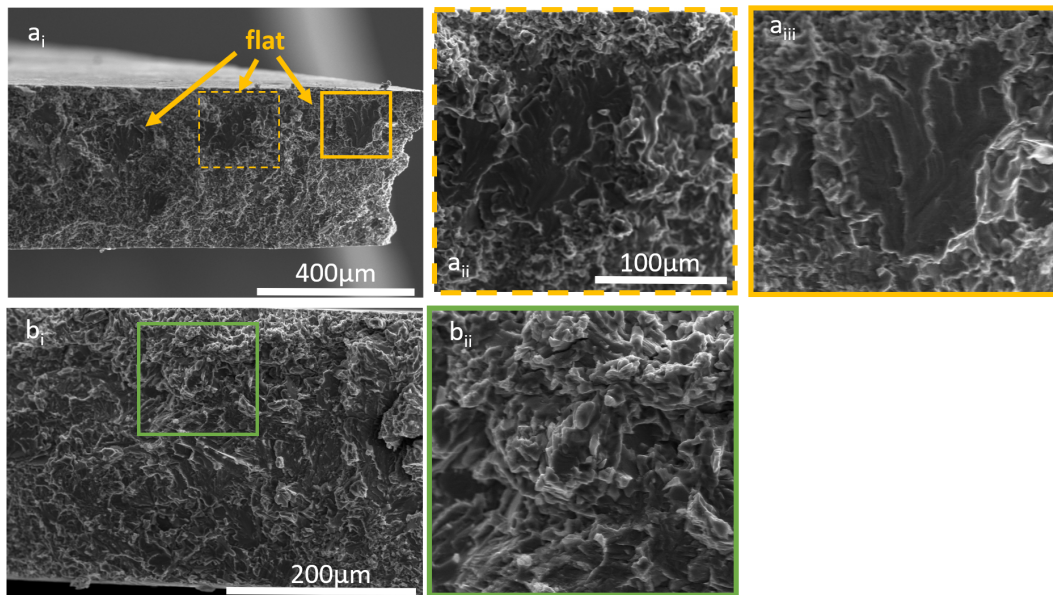


Figure 4.8: SEM images showing the microstructure of the pressed sample P-Pow-3. a_i : The full width of the fracture surface cross section, showing three flat looking areas. a_{ii} : Magnification of the dashed yellow square showing a flat looking area surrounded by a rough textured surface. a_{iii} : Magnification of the solid line yellow square showing a flat looking area surrounded by a rough textured surface. b_i : Showing the rough looking texture that is present around the flat looking areas of the cross section. b_{ii} : Magnification of the green square reveal smooth texture.

4.3 Crystallographic information of crystal powder and pressed samples

To determine the crystal structure and majority phase of the prepared materials XRD and subsequent Rietveld-refinement was performed. Experiments were performed on both crushed powders and pressed samples (Table 3.1) to identify potential influence of the various processing methods of the material. The XRD patterns of the two powder samples (C-Pow-1 and C-Pow-2), the four pressed agglomerate samples (P-Agl-1, P-Agl-2, P-Agl-3 and P-Agl-4) and the four pressed powder samples (P-Pow-1, P-Pow-2, P-Pow-3, and P-Pow-4) are shown in Figure 4.9. The estimate percentage of the majority phase, obtained from Rietveld-refinement, is seen above each sample diffractogram, in corresponding legend colour. However, there is a large degree of overlap between the peaks of the Cmc_m and Amm2 phase, which makes accurate quantitative phase ratio determination difficult, especially when a 10 wt% uncertainty in phase percentage determination from laboratory XRD is expected. Due to the large overlap between the diffraction lines of the two contributing phases, only the main peaks of the majority phase are labelled with the Miller indices of the normal of the plane of diffraction up to 35 degrees 2θ , while the minority phase contributions are marked with either a \bullet or \blacktriangle for the Cmc_m and Amm2 as minority phase, respectively. Selected results are summarised in Table 4.1, and described in the following paragraphs.

Table 4.1: Parameters from XRD-data

| Sample | Majority phase | a(Å) | b(Å) | c(Å) | Secondary phase | GOF |
|---------|------------------|-------|-------|--------|---------------------------------|------|
| C-Pow-1 | Amm2 | 7.257 | 9,030 | 9,360 | - | 2.97 |
| C-Pow-2 | Amm2 | 7.225 | 9,030 | 9,354 | - | 3.02 |
| P-Agl-1 | Amm2 | 7.223 | 9.000 | 9.320 | Cmc _m (\sim 17 %) | 4.72 |
| P-Agl-2 | Amm2 | 7.260 | 9.028 | 9.355 | Cmc _m (\sim 32 %) | 3.54 |
| P-Agl-3 | Cmc _m | 8.935 | 9.628 | 14.257 | Amm2 (\sim 48 %) | 3.93 |
| P-Agl-4 | Unidentified | - | - | - | - | - |
| P-Pow-1 | Cmc _m | 8.943 | 9.632 | 14.287 | Amm2 (\sim 9 %) | 4.20 |
| P-Pow-2 | Cmc _m | 8.947 | 9.636 | 14.283 | Amm2 (\sim 7 %) | 5.63 |
| P-Pow-3 | Cmc _m | 8.944 | 9.631 | 14.291 | Amm2 (\sim 12 %) | 4.22 |
| P-Pow-4 | Cmc _m | 8.944 | 9.635 | 14.279 | Amm2 (\sim 10 %), | 4.41 |

The XRD pattern indicate that the powdered samples are purely Amm2 phase. The pressed agglomerate samples P-Agl-1 and P-Agl-2 were found to have Amm2 as majority phase, making up approximately 83 wt% and 68 wt%, respectively. The Cmc_m-phase makes up the majority of the pressed agglomerate P-Agl-3 sample (58% Cmc_m), as well as for all four samples pressed from powder; P-Pow-1 (91% Cmc_m), P-Pow-2 (93% Cmc_m), P-Pow-3 (88 wt% Cmc_m) and P-Pow-4 (90 wt% Cmc_m). Selected results are included in Table 4.1. Relative diffraction line intensities vary a little between the samples, but distinct patterns have not been identified. For the XRD pattern of the pressed agglomerate sample P-Agl-4, the results from the fits towards Amm2 and Cmc_m did not give convincing results about the majority phase. Repeated measurements and fitting towards Pma2 did not give conclusive results either. All peaks below 18 degree 2θ are missing from the diffractogram. For Amm2 this would include the (100) and (011) planes normals, while for Cmc_m it would include (022), (110) and (111) planes normals of the Cmc_m-phase.

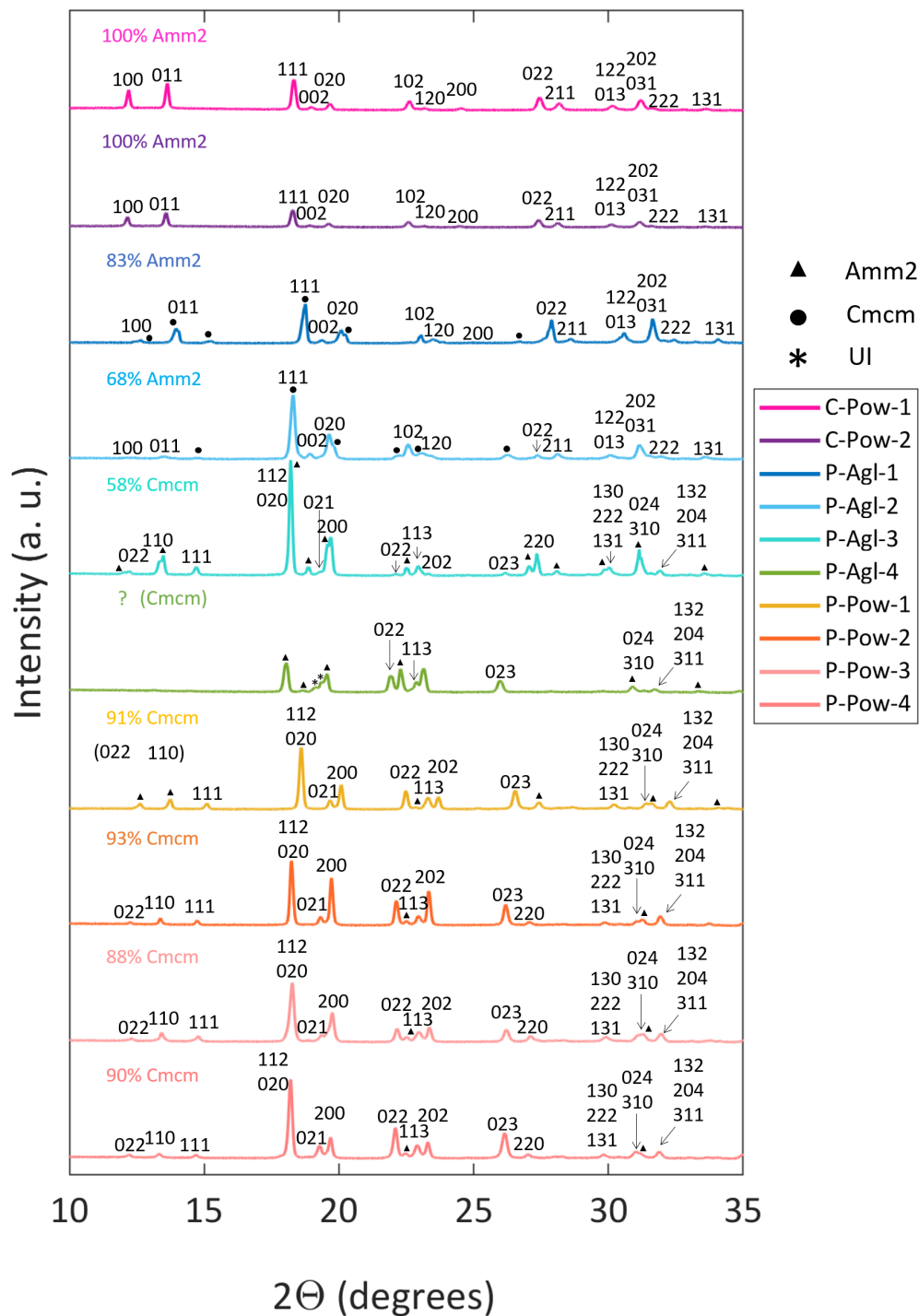


Figure 4.9: XRD patterns of the eight pressed samples from 10 and 35 2θ . For sample C-Pow-2, P-Agl-1 and P-Agl-2 the majority phase is Amm2, while in sample P-Pow-1, P-Pow-2, P-Pow-3 and P-Pow-4 the majority phase is Cmcmm. The P-Agl-4 samples majority phase is not identified. In all sample diffractograms, the majority phase contribution is marked with Miller indices (hkl), while the minority phase contribution is marked with a \blacktriangle or \bullet for Amm2 and Cmcmm as minority phase, respectively. The amount (wt%) of the majority phase is included above the respective diffractogram, in the corresponding legend colour.

4.4 Vibrational spectroscopy

4.4.1 Raman

The resulting spectra of the temperature dependent Raman series, which was performed on sample P-Agl-1, are presented in Figure 4.10. They include bands originating from both the inorganic FeBrCl_3 anion, present below 400 cm^{-1} , and the organic TMA cation, associated with the bands at higher wavenumbers. The full range of the average Raman spectra within the temperature series can be seen in Figure 4.10 a. A closer look at the bands below 500 cm^{-1} is done in Figure 4.10 b, and the bands located at high $2700\text{-}3200 \text{ cm}^{-1}$ can be observed in Figure 4.10 c. Assignment of the bands present in the spectra is based on literature and the results are summarised in Table 4.2. All spectra before and after CRR processing is presented in Appendix A.1 Figure A.1

Table 4.2: Results from Raman and Infrared spectroscopy studies.

| Raman(cm^{-1}) | | | IR(cm^{-1}) | | | | Assignment |
|---------------------------|----------|----------|------------------------|-------------|----------|------------|--|
| P-Agl-1 | | | P-Agl-1 | P-Agl-2 | P-Pow-1 | P-Pow-2 | |
| 30 °C | 80 °C | 125 °C | | | | | |
| 101(b) | 101(b) | 101(b) | | | | | ν_2 and ν_4 of FeBrCl_3 [35] |
| 206(sh) | - | - | | | | | Fe-Br (asym.?) [25, 30] |
| 227(s) | 227(s) | 227(s) | | | | | FeBrCl_3 asym. [25, 30] |
| 247(s+) | 247(s+) | 247(s+) | | | | | Fe-Br sym. stretch [25, 30] |
| 267(s) | 267(s) | 267(s) | | | | | Fe-Br sym. stretch [25, 30] |
| 294(sh) | * | - | | | | | Fe-Br asym. stretch [25, 30] |
| 334(m) | 334(m) | 334(m) | | | | | Fe-Cl sym. stretch [25, 30] |
| 351(w) | 351(w) | 351(w) | | | | | Fe-Cl sym stretch [25, 30] |
| | | | 372(s) | 372(s) | 372(s) | 372(s) | C_4N asym. deform. [31, 33] |
| 395(b) | 395(b) | 395(b) | | | | | Fe-Cl asym. stretch [25, 30, 36] |
| 454(w) | | | | | | 729(m) | C_4N asym. stretch [31–33] |
| | | | - | - | - | | C_4N sym. stretch [33] |
| 752(w) | 752(w) | 752(w) | | | | | C_4N sym. stretch[25, 31–33] |
| | | | 914(sh) | 914(sh) | 914(sh) | 914(sh) | C_4N asym. stretch[31] |
| 948(w) | 948(w) | 948(w) | | | | | C_4N asym. stretch [25, 31–33] |
| | | | 1065(w) | 1065(w) | 1065(w) | 1065(sh) | CH_3 rock. [31] |
| | | | 1284(m) | 1284(m) | 1284(m) | 1284(m,sh) | CH_3 rock. [25, 31, 33] |
| | | | 1414(m+) | 1414(m+) | 1414(m+) | 1414(m+) | CH_3 sym. deform. [31, 33] |
| 1450(w) | 1450(w) | 1450(w) | | | | | CH_3 asym. deform.[25, 31–33] |
| 1477(w-) | 1477(w-) | 1477(w-) | 1477(s) | 1477(s) | 1477(s) | 1477(s) | CH_3 asym. deform. [31, 33] |
| | | | - | - | - | 1718(s) | CH_3 torsion +asym. deform. [31] |
| 2440(w) | 2440(w) | 2440(w) | | | | | CH_3 rock. + asym. deform. [31, 32] |
| | | | 2478(w) | 2478(w) | 2478(w) | 2478(w) | CH_3 rock. + asym deform. [31] |
| | | | 2579(w) | 2579(w) | 2579(w) | 2579(w) | CH_3 rock. + asym. deform. [31] |
| | | | 2750(w) | 2750(w) | 2750(w) | 2750(w) | CH_3 rock. + asym. deform. [31] |
| 2815(m) | 2815(m) | 2815(m) | | | | | CH_3 sym. deform [33]/ |
| | | | | | | | CH_3 sym. +asym. deform. [31, 32] |
| 2923 | 2923 | 2923 | 2853(w) | 2853(m) | - | - | CH_3 sym. + asym. deform. [31] |
| | | | | | | | CH_3 asym. deform.[33] / |
| | | | | | | | CH_3 sym stretch [31, 32] |
| 2952(m) | 2952(m) | 2952(m) | 2924(m) | 2924(m+) | - | - | C–H sym. strech [31, 33] |
| | | | | | | | C–H sym. strech [33]/ |
| | | | | | | | CH_3 asym. deform [31, 32, 37] |
| | | | 2961(w) | 2961(sh,w-) | 2961(m) | 2961(m) | C–H sym. stretch [33]/ |
| 2976(m) | 2976(m) | 2976(m) | | | | | CH_3 asym. deform.[31] |
| | | | | | | | CH_3 sym. stretch[33]/ |
| | | | | | | | CH_3 asym. deform[31, 32] |
| 3029(m) | 3029(m) | 3029(m) | 3022(m) | 3022(m) | 3022(m) | 3022(m) | C–H asym. stretch [31–33, 37] |

Intensity of peak: weak (w), middle (m), strong (s), more (+), less (-)

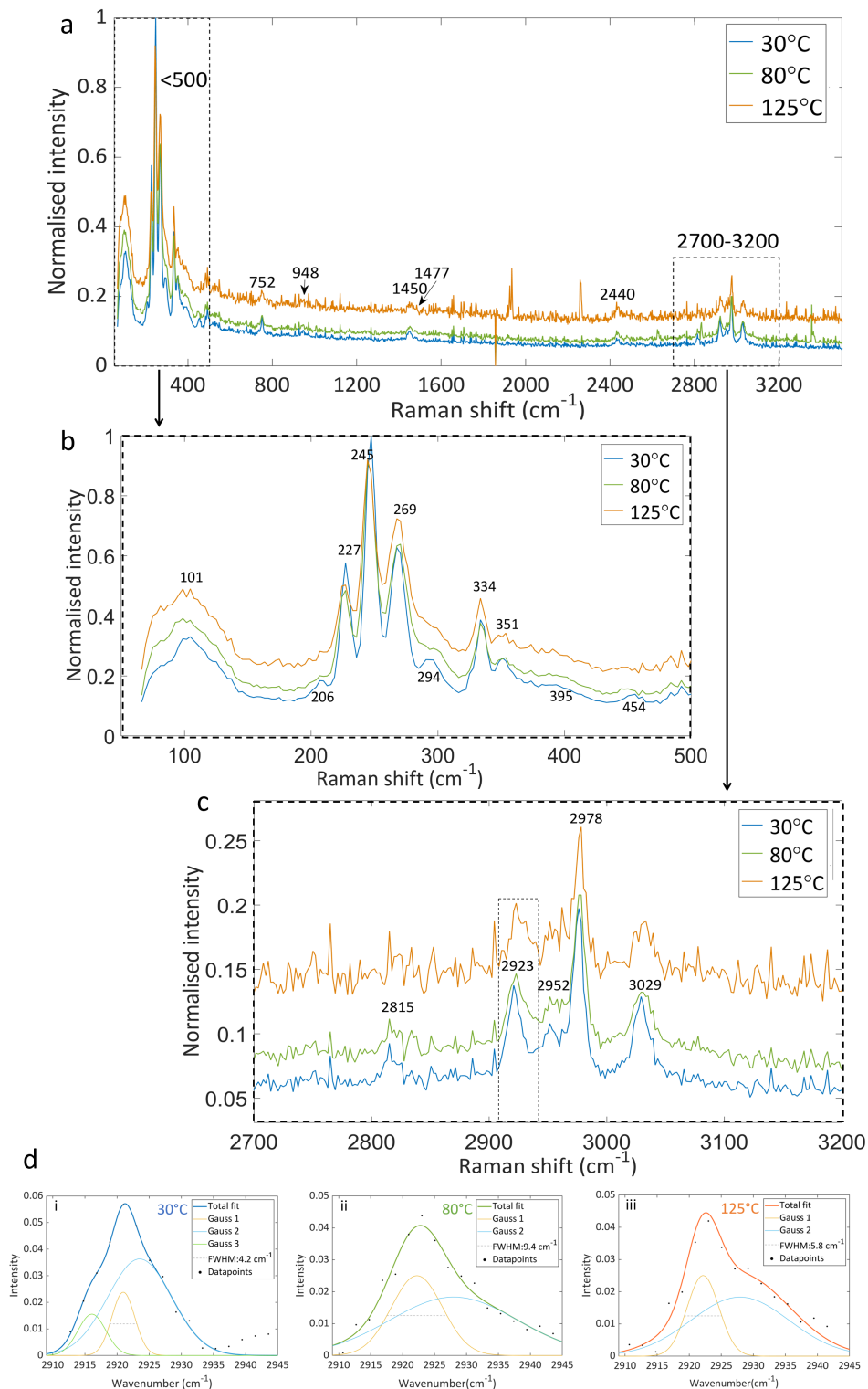


Figure 4.10: Raman spectra for sample P-Agl-1. a: Average spectra from temperature series at 30 °C, 80 °C and 125 °C between 50 and 3400 cm^{-1} . b: Low wavenumber range (50-500 cm^{-1}). c: High wavenumber range (2700-3200 cm^{-1}). d: Band fitting and FWHM estimation for the 2923 cm^{-1} band at *i*: 30 °C *ii*: 80 °C and *iii*: 125 °C.

All the bands present at wavenumbers lower than 400 cm^{-1} (Figure 4.10 b) origin from the inorganic anion FeBrCl_3 [25, 30, 36]. The broad band observed at 101 cm^{-1} could be associated with either the ν_2 or ν_4 mode of the FeBrCl_3 anion [35]. The strong bands at 227, 247 and 267 cm^{-1} , as well as the two shoulders at 206 and 294 cm^{-1} are likely to be associated with symmetric and asymmetric stretching of Fe-Br, respectively [25, 30]. It is observed that the two shoulders decrease in intensity with increased temperature. The signals present at 334 and 351 cm^{-1} are probably related to the symmetric stretching of Fe-Cl, while the the broad band centred at 395 cm^{-1} could be caused by asymmetric stretching of the same band [25, 30].

At wavenumbers above 400 cm^{-1} , the bands origin from the organic cation TMA, which include vibration modes associated with C_4N skeleton of the cation as well as its methyl groups ($-\text{CH}_3$) [25, 30, 31]. In Figure 4.10 b there is a small band noted, only at room temperature, at 454 cm^{-1} which is likely to be the asymmetric deformation of C_4N . Again C_4N are probably related to the bands at 752 cm^{-1} , caused by symmetrical stretching and at 948 cm^{-1} , linked to asymmetrical stretching (Figure 4.10 a) [25, 31–33]. The bands present at wavenumbers above 1000 cm^{-1} is assigned to the methyl ($-\text{CH}_3$) groups. The bands at 1450 and 1477 cm^{-1} are both related to asymmetric deformation (Figure 4.10 a). At 3029 cm^{-1} the signal is caused by asymmetric stretching of C-H (Figure 4.10 c). For the bands at 2815, 2923, 2952 and 2976 cm^{-1} literature does not agree on what vibrating mechanism of the methyl group that give the mentioned band signals.

The band at 2923 cm^{-1} broadens with increasing temperature, and fitting with Gaussian curves (Figure 4.10 d) shows us that this band at $30\text{ }^\circ\text{C}$ (d_i) can be deconvoluted to contain three Gaussian curves, while at $80\text{ }^\circ\text{C}$ (d_{ii}) and $125\text{ }^\circ\text{C}$ (d_{iii}), the leftmost band no longer contributes. The FWHM of the main peak (yellow line) was found to be 4.2, 9.4 and 5.8 cm^{-1} at the three temperatures, in increasing order. The rightmost band drops in intensity and broaden at 80 and $125\text{ }^\circ\text{C}$ compared to $30\text{ }^\circ\text{C}$.

4.4.2 Infrared spectroscopy

To support Raman and XRD analysis by giving information on vibrational bands that are not Raman active ATR IR spectroscopy was performed on the pressed agglomerate samples P-Agl-1 and P-Agl-2, as well as the pressed powder samples P-Pow-1 and P-Pow-2 (Table 3.1). The IR spectra in the range $350\text{--}3400\text{ cm}^{-1}$ in Figure 4.11 a and all the results are summarised in Table 4.2. This includes vibrations modes related to the C_4N skeleton of the cation as well as its methyl groups ($-\text{CH}_3$). C_4N are likely to give the bands at 372 cm^{-1} , associated to asymmetric deformation, the weak band at 729 cm^{-1} , assigned to symmetrical stretching, in addition to the shoulder at 914 and strong peak 944 cm^{-1} , both caused to asymmetrical stretching [25, 31, 33]. The band at 729 cm^{-1} is only present in the spectrum of P-Pow-2. The methyl groups give rise to all the bands identified above 1000 cm^{-1} [31, 33]. Rocking of the methyl group is likely to give the weak bands at 1065 and 1284 cm^{-1} , symmetric deformation is cause of the shoulder at 1414 cm^{-1} , and asymmetric deformation gives the strong bands at 1477 cm^{-1} [25, 31, 33]. Some bands are assigned to a combination of two modes. The band at 1718 cm^{-1} , only present in sample P-Pow-2, could origin from CH_3 torsion as well as asymmetric deformation [31], while the very weak bands at 2478, 2579 and 2750 cm^{-1} can relate to the combination of rocking and asymmetric deformation of the methyl group. A closer look at the $2400\text{--}3100\text{ cm}^{-1}$ range is seen in Figure 4.11 b. The band at 2853 cm^{-1} is likely to come from both asymmetric and symmetric deformation of the same group. Symmetric and asymmetric C-H stretching within the methyl group could create the moderate and weak signals

at 2924 and 3022 cm^{-1} , respectively [31, 33]. For the weak band at 2961 cm^{-1} literature suggests both symmetric stretching of the C-H band [33], as well as asymmetric deformation of the methyl groups [31] as possible cause. The bands at 2853 and 2924 cm^{-1} are only present in the pressed agglomerate samples, P-Agl-1 and P-Agl-2. Some unidentified peaks are also worth mentioning, as they are distinct for some of the spectra. In the spectra of the P-Pow-1 and P-Pow-2 samples, a weak band is present at 1264 cm^{-1} (not labelled). A weak band is present at 887 cm^{-1} in the samples P-Agl-2 and P-Pow-2 (not labelled). And P-Pow-2 also has a band at 1101 cm^{-1} (not labelled).

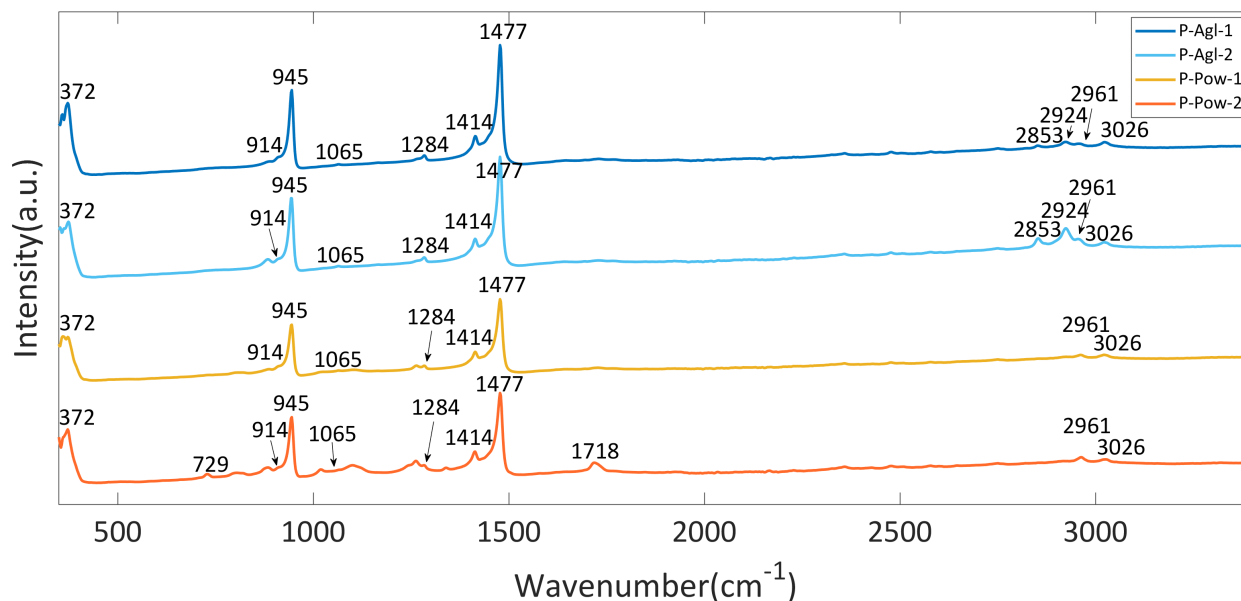


Figure 4.11: Infrared spectra from the samples P-Agl-1, P-Agl-2, P-Pow-1 and P-Pow-2. a: Full range of the spectra from 350-3400 cm^{-1} . b: Spectra within dashed square (2400-3100 cm^{-1}).

4.5 Phase transitions

DSC measurements were done on one powder sample (C-Pow-2), two pressed agglomerate samples (P-Agl-2 and P-Agl-) and two pressed powder samples (P-Pow-2 and P-Pow-3), described in Table 3.1. The intention of the DSC experiment was to provide thermodynamic information of the phase transitions of the system that could also help support the phase distinctions made using the structural characterisation techniques, in particular XRD. All these samples were first run for two consecutive cycles between -25 and 200 $^{\circ}\text{C}$, by heating and cooling at 10 $^{\circ}\text{C}/\text{min}$, before one of each sample type, C-Pow-2, P-Agl-1 and P-Pow-2 later was run for another four consecutive cycles. The data for each sample can be seen in Figure 4.12 and the results are summarised in Table 4.3.

Figure 4.12 a shows the DSC data for the crushed powder sample, C-Pow-2. Four transitions peaks are observed upon heating. In the first cycle (purple line) these are located at -10, 8, 88 and 110 $^{\circ}\text{C}$. The transitions upon heating were all endothermic and are signs of the polymorphic transition of the material from the phase Pbcm to Pma2 (V-IV), Pma2 to Amm2 (IV-III), Amm2 to Cmcm (III-II) and Cmcm to Pm $\bar{3}$ m (II-I). The transition into the plastic crystal mesophase Pm $\bar{3}$ m holds the largest change in both enthalpy, seen by the large intensity of the peak, and entropy, indicated by the area under the peak. The high entropy change observed is associated with the rotational freedom achieved by the organic cations in the plastic crystal mesophase being released in the

transition.

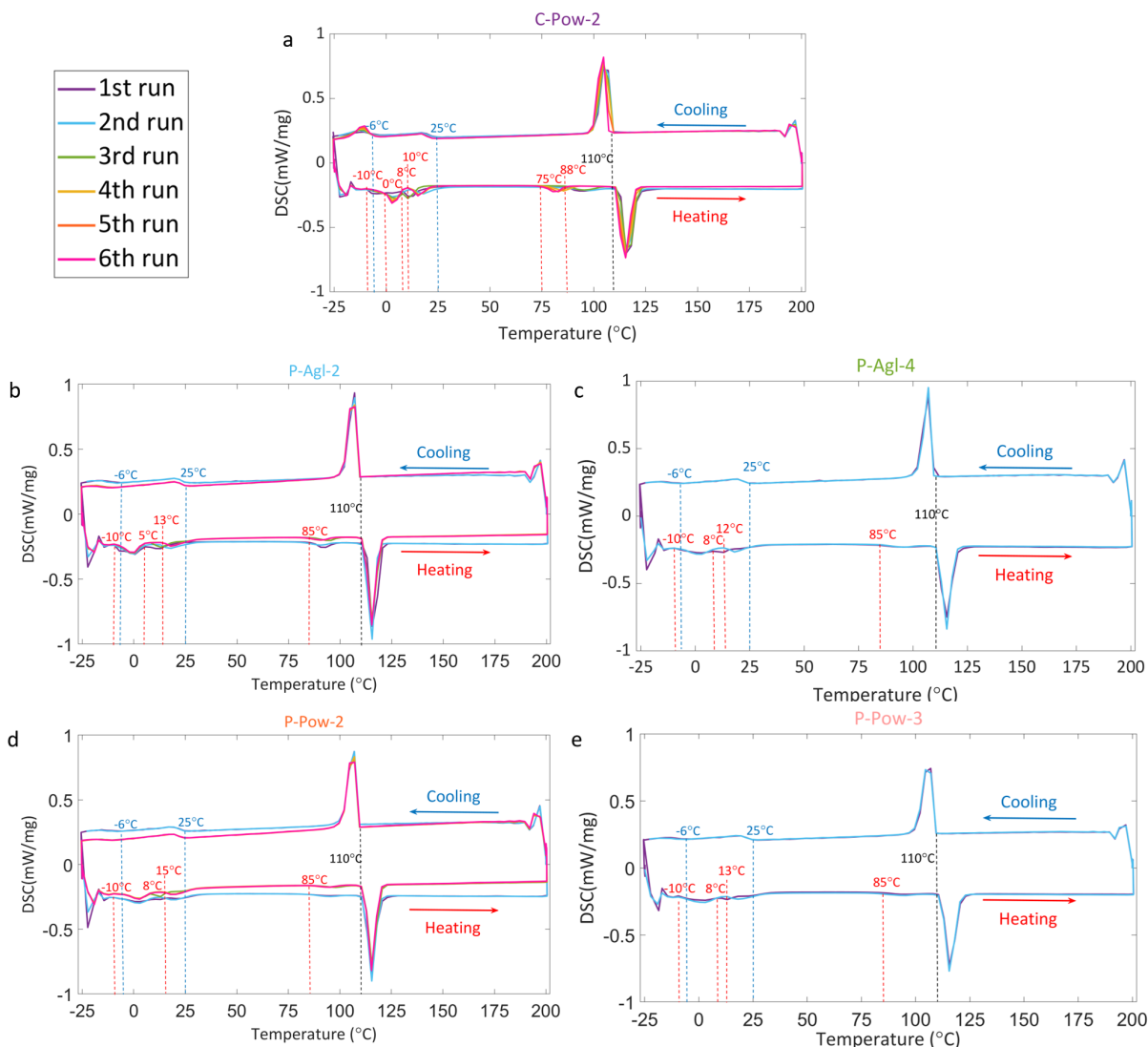


Figure 4.12: DSC results for crystal powder sample a: C-Pow-2, the pressed agglomerate samples b: P-Agl-2 and c: P-Agl-4 and the pressed powder sample d: P-Pow-2 and e: P-Pow-3. The samples were cycled between $-25\text{ }^{\circ}\text{C}$ and $200\text{ }^{\circ}\text{C}$. First to consecutive cycles were run for all samples and then later four additional cycles were run for the the three samples C-Pow-2, P-Agl-2 and P-Pow-2.

Then upon cooling the reversed transition from plastic crystal mesophase to Cmcm (I-II) occurs at the same temperature and is of the same magnitude. The next transition (II-III) show a much larger hysteresis and does not occur before the system is cooled to $25\text{ }^{\circ}\text{C}$. This is slow and diffuse followed by a tail leading, likely to have obscured the III-IV transition, in to the next and last clear transition peak at $-6\text{ }^{\circ}\text{C}$, belonging to the IV-V transition. Upon repeated cycling the same transition behaviour is observed, however some variation is seen in the following five cycles and is detailed as follows. The I-II transition (on heating) is shifted to $0\text{ }^{\circ}\text{C}$ in run 2-6. In cycle 2 and 4-6 the II-III transition (on heating) has onset at $15\text{ }^{\circ}\text{C}$, being higher than for cycle 1 and 3. Upon the fourth through sixth cycle the III-II transition shifts to a lower onset at $75\text{ }^{\circ}\text{C}$ and happens

over a narrower temperature range. The on cooling transition from the plastic crystal mesophase (I-II) is stable at 110 °C for all cycles except for in the sixth run where the onset happens at 107 °C.

Table 4.3: Transition temperatures from DSC

| Sample | Cycle | V-IV | IV-III | III-II | II-I | I-II | II-III | IV-V |
|----------------|-------|------|--------|--------|------|------|--------|------|
| C-Pow-2 | 1 | -10 | 8 | 88 | 110 | 110 | 25 | -6 |
| | 2 | 0 | 15 | 88 | 110 | 110 | 25 | -6 |
| | 3 | 0 | 8 | 88 | 110 | 110 | 25 | -6 |
| | 4 | 0 | 15 | 75 | 110 | 110 | 25 | -6 |
| | 5 | 0 | 15 | 75 | 110 | 110 | 25 | -6 |
| | 6 | 0 | 15 | 75 | 110 | 107 | 25 | -6 |
| P-Agl-2 | 1 | -10 | 5 | 85 | 110 | 110 | 25 | -6 |
| | 2 | -10 | 13 | 85 | 110 | 110 | 25 | -6 |
| | 3 | -10 | 8 | 85 | 110 | 110 | 25 | -6 |
| | 4 | -10 | 13 | 85 | 110 | 110 | 25 | -6 |
| | 5 | -10 | 13 | 85 | 110 | 110 | 25 | -6 |
| | 6 | -10 | 13 | 85 | 110 | 110 | 25 | -6 |
| P-Agl-4 | 1 | -10 | 12 | 85 | 110 | 112 | 25 | -6 |
| | 2 | -10 | 8 | 85 | 110 | 109 | 25 | -6 |
| P-Pow-2 | 1 | -10 | 8 | 85 | 110 | 110 | 25 | -6 |
| | 2 | -10 | 15 | 85 | 110 | 110 | 25 | -6 |
| | 3 | -10 | 8 | 85 | 110 | 110 | 25 | -6 |
| | 4 | -10 | 15 | 85 | 110 | 110 | 25 | -6 |
| | 5 | -10 | 15 | 85 | 110 | 110 | 25 | -6 |
| | 6 | -10 | 15 | 85 | 110 | 110 | 25 | -6 |
| P-Pow-3 | 1 | -10 | 8 | 85 | 110 | 110 | 25 | -6 |
| | 2 | -10 | 13 | 85 | 110 | 110 | 25 | -6 |

In Figure 4.12 b-e the behaviour of the pressed samples P-Agl-2, P-Agl-4, P-Pow-2 and P-Pow-3 upon heating and cooling can be observed, respectively. It is fairly similar to the one of C-Pow-2. Upon heating the following differences are noted: The V-IV transition stays stable at -10 °C through all cycles for all the pressed samples. For the IV-III transition variation is seen in all pressed samples except P-Pow-2 (Figure 4.12 d), where for sample P-Agl-2 (Figure 4.12 b) the onset of the transition happens at 5 and 8 °C for the 1st and 3rd run, and at 13 °C for the 2 and 4-6th run. For P-Agl-4 (Figure 4.12 c) the transition shifts from 12 to 8 °C for the first and second cycle respectively. This is the only sample where the shift between first and second cycle is to lower temperatures. For sample P-Pow-3 (Figure 4.12 e) there is a shift from 8 to 13 °C for the 1st and 2nd cycle, respectively. The third transition (III-II) is fixed at 85 °C for all the pressed samples, however, the transition is very diffuse, if present at all, for all pressed samples except P-Agl-2. The variations during cooling are described next. The I-II transition is very stable at 110 degrees for the pressed samples, but small shifts of the onset to 112 and 109 for the first and second cycle of sample P-Agl-4 are present. The IV-V transition stays stable at -6 °C for all cycles in all samples, however the transition peak is more diffuse for all the pressed samples than in the powder sample C-Pow-2.

4.6 Results from I-V measurements and P-E, I-E and S-E hysteresis measurements

Electrical measurements were performed to characterise the electrical leakage and ferroelectric properties of the materials. Current-voltage (I-V) measurements, at low fields (10 or 20 kV/cm) were used to quantify the leakage currents while polarisation (P), current (I) and strain (S) hysteresis as a function of electric field amplitude (1-400 kV/cm) and frequency (100-1 Hz) was used to characterise the ferroelectric behaviour. The electrical measurements were carried out on the three pressed agglomerate samples, P-Agl-1, P-Agl-2 and P-Agl-4, as well as two pressed powdered samples P-Pow-1 and P-Pow-2. Selected results of all the measurements are collected in Table 4.4.

Table 4.4: Parameters from I-V, P-E,

| Parameter | P-Agl-1 | P-Agl-2 | P-Agl-4 | P-Pow-1 | P-Pow-2 |
|---|------------|-------------|-------------|---------|-------------|
| Thickness (mm) | 0.28 | 0.38 | 0.19 | 0.15 | 0.28 |
| I_{Lb} at 10kV/cm ($\mu\text{A}/\text{cm}^2$) | 0.27 | 0.49 | 0.20 | 0.09 | 0.19 |
| I_{La} at 10kV/cm ($\mu\text{A}/\text{cm}^2$) | 0.34 | 1.01 | 0.34 | 0.21 | 1.43 |
| change before and after at 10 kV/cm (%) | 20 | 51 | 40 | 57 | 87 |
| Max field (kV/cm) | 200 | 260 | 300 | 450 | 290 |
| P_r at 200 kV/cm ($\mu\text{C}/\text{cm}^2$) | 2.2 | 3.3 | 5 | 3.5 | 7 |
| P_r at max field ($\mu\text{C}/\text{cm}^2$) | " | 4.3 | 9.3 | 1.2 | 25(-37) |
| E_c at 200 kV/cm (kV/cm) | 150 | 116 | 125 | 130 | 130 |
| E_c at max field (kV/cm) | " | 138 | 219 | 318 | 252 |
| I_{Peak} at 200 kV/cm (A/m) | 0.24 | 0.36 | 0.69 | 0.01 | 0.62 |
| Field of I_{Peak} at 200 (kV/cm) | 146 | 106 | 104 | 196(?) | 84 |
| I_{Peak} at max field (A/m) | " | 0.42 | 0.9 | 0.16 | 1 |
| Field of acrsHORTIp at max field (kV/cm) | " | 115 | 117 | 282 | 90 |
| S_{PP} at 200 kV/cm (%) | ~ 0.1 | ~ 0.08 | ~ 0.08 | (?) | ~ 0.06 |
| S_{PP} at max field (%) | " | ~ 0.1 | ~ 1.5 | (?) | ~ 1.8 |

4.6.1 Current-voltage data

I-V measurements were done before and after driving the pressed sample to high fields, with the intention to compare the leakage present in the samples before and after cycling. However, as the electrical history of each sample is not exactly the same, due to different amount of cycling, the comparison can only be considered qualitatively. Selected results are summarised in Table 4.4. The current-voltage data acquired before and after cycling at high fields from the pressed samples P-Agl-1, P-Agl-2, P-Agl-4, P-Pow-1 and P-Pow-2 are presented Figure 4.13 a-e, respectively. An increase from observed leakage current density before (I_{Lb}) to the the observed leakage current density after (I_{La}) occurs in all samples upon cycling. Further it is noted that the largest change occurs in the P-Pow-2 sample, being in a full order of magnitude. The change before and after cycling in all the samples is also illustrated in Figure 4.14, where the absolute leakage current before and after cycling at 10 kV/cm for each of the five samples is shown in a barplot. The leakage current of P-Agl-1 changes from 0.27 to 0.34 $\mu\text{A}/\text{cm}^2$ before and after cycling, for P-Agl-2 the change was from 0.49 to 1.01 $\mu\text{A}/\text{cm}^2$ and for P-Agl-4 the absolute current density increased from 0.2 to 0.34 $\mu\text{A}/\text{cm}^2$. This gives a 25, 106 and 70 % increase, respectively. A change from 0.09 to 0.21 $\mu\text{A}/\text{cm}^2$ and from 0.19 to 1.43 $\mu\text{A}/\text{cm}^2$, gives a 133 and 653 % increase in leakage current present in the powdered samples P-Pow-1 and P-Pow-2, respectively. For sample P-Pow-1, where current-voltage data was collected between -20 and +20 kV/cm, the first 10 kV/cm datapoint in the cycle was used.

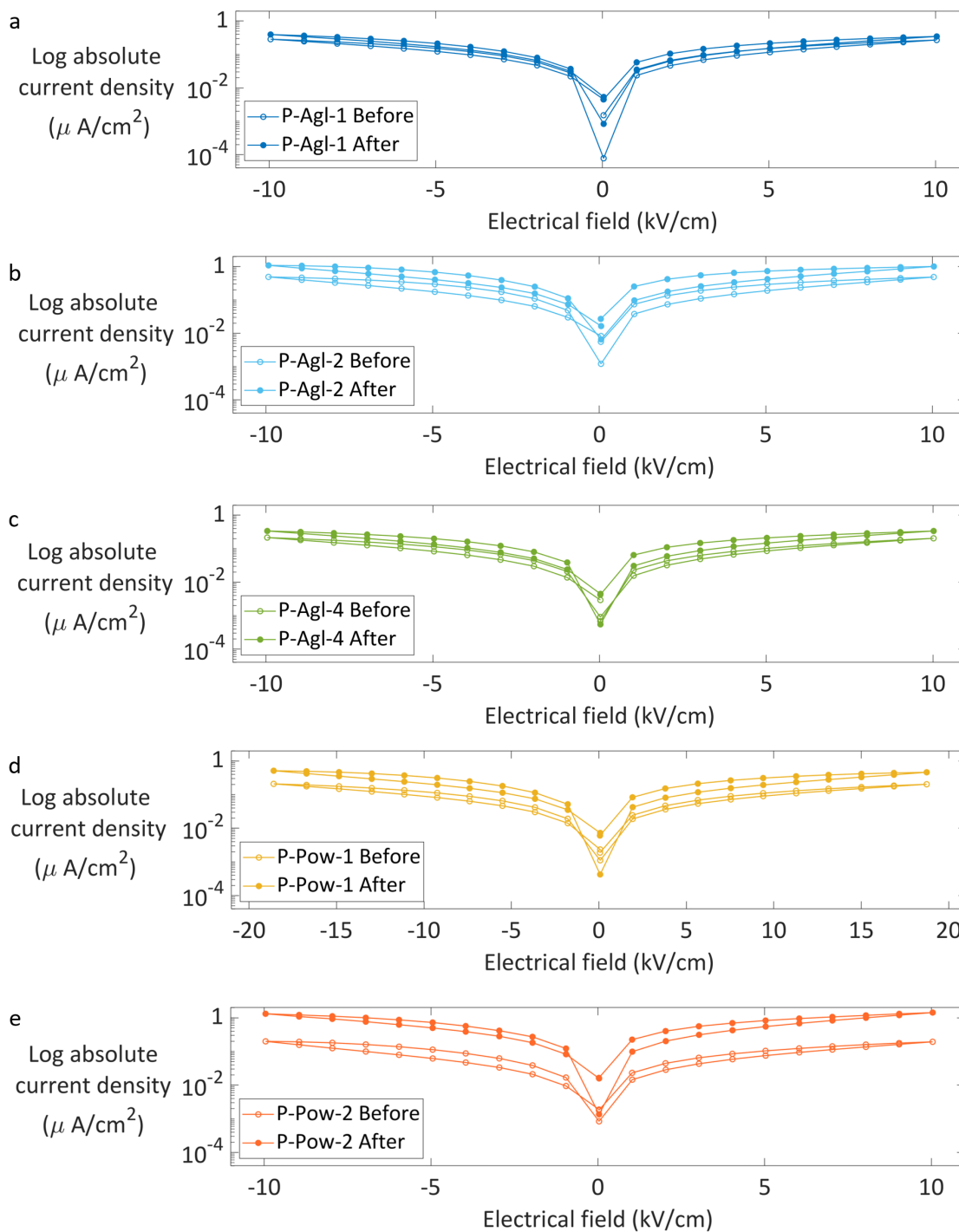


Figure 4.13: Current-Voltage measurements of the samples a: P-Agl-1, b: P-Agl-2 c: P-Agl-4, d: P-Pow-1 and e: P-Pow-2 where the absolute current density is plotted on a logarithmic scale. Similar leakage current measurement were performed before and after cycling at stepwise increasing electrical fields. The before and after data is represented by unfilled and filled datapoints, respectively.

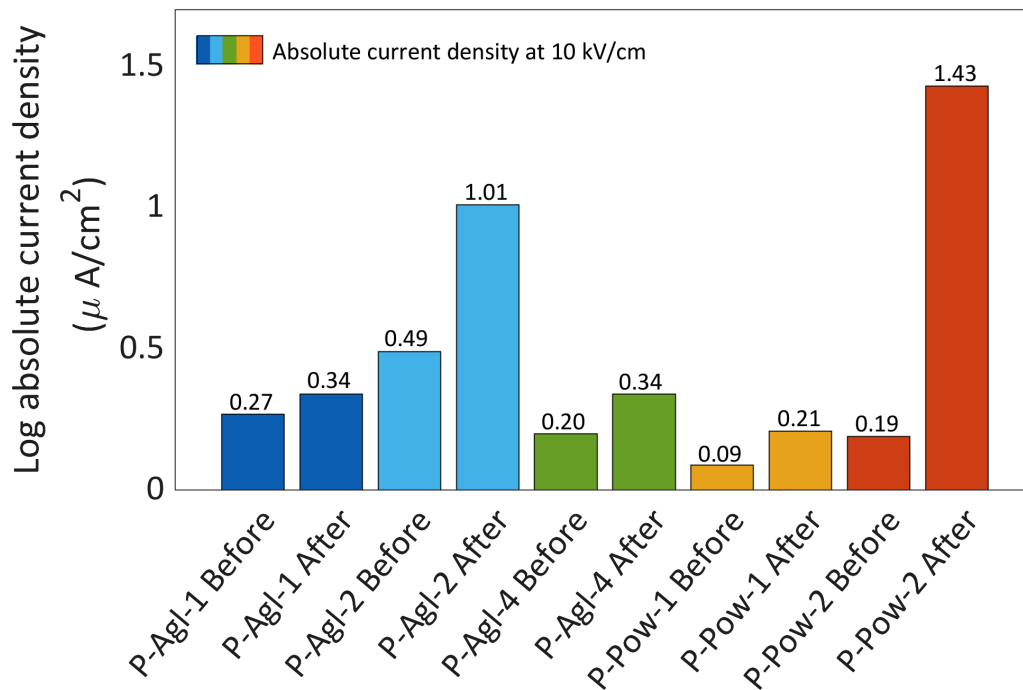


Figure 4.14: Absolute current density at 10 kV/cm for the samples P-Agl-1 (blue), P-Agl-2 (light blue), P-Agl-4 (green), P-Pow-1 (yellow) and P-Pow-2 (orange), before and after cycling showed in a barplot.

4.6.2 Polarisation, current density and strain loops

The five samples were first cycled with stepwise increased electric fields up to 200 kV/cm (400 kV/cm for P-Pow-1), the P-E, I-E and S-E hysteresis behaviour was recorded and is shown, for comparison, in Figure 4.15. Selected data is also summarised in Table 4.4. To see the polarisation, current density and strain data for each sample at maximum electrical field, the reader is referred to Appendix A.2. The samples were driven to maximum fields of 200, 260, 290, 400 and 300 kV/cm in the following order; P-Agl-1, P-Agl-2, P-Agl-4, P-Pow-1 and P-Pow-2.

Figure 4.15 shows that the pressed agglomerate samples, P-Agl-1 (a), P-Agl-2 (b), and P-Agl-4 (c), show P-E(*i*), I-E(*ii*) and S-E(*iii*) behaviour at 200 kV/cm being characteristic of ferroelectrics. The P_r are 2.2, 3.3 and 5 $\mu\text{C}/\text{cm}^2$, the E_c are 150, 116 and 125 kV/cm and the S_{PP} are ~ 0.1 , 0.08 and 0.08 for the three of them respectively. At 200 kV/cm the current density loops peak at 146 and -132 kV/cm with the values 0.24 and -0.22 A/m, respectively for the P-Agl-1 sample. For the P-Agl-2 sample the peaks lie at 106 and -102 kV/cm and have the values 0.36 and 0.32 A/m. For P-Agl-4 they occur at 104 and -102 kV/cm with 0.69 and 0.65 A/m. The P-Pow-1 sample does not show specific ferroelectric behaviour at 200 kV/cm, but opens up at higher fields (Appendix A.2 Figure A.2). However, the following parameters are noted; P_r is 3.5 $\mu\text{C}/\text{cm}^2$ and E_c is 130 kV/cm. The strain loops of the sample does not follow the characteristic butterfly loop, but rather a S-shaped curve that could be caused by drift. The pressed powder sample P-Pow-2 also shows P-E, I-E and S-E behaviour that is characteristic of a ferroelectric material. It has a P_r of 7 $\mu\text{C}/\text{cm}^2$ and a E_c of 130 kV/cm. Between cycling at 150 and 160 kV/cm there is a gap, where

the polarisation and current density as a function of field increases more than between the last steps. This is likely to be caused by repeated cycling, 3 times, at 160 kV/cm as the measurement current range was overloaded two times before adjusted correctly. The sample's strain experiences some drift, indicated by the S-shape of the loop, before stabilising in a butterfly shaped loop at higher fields. At 200 kV/cm the S_{PP} is $\sim 0.06\%$. The current density loop peaks at ± 84 and has the values 0.62 and -0.59.

Subsequently all the samples were studied while the frequency of the electrical field was varied between 100 and 1 Hz (Figure 4.16). For sample P-Agl-1(a), P-Agl-2(b), and P-Agl-4(c), as well as P-Pow-2(e) the frequency sweep carried out at 200 kV/cm, while for the P-Pow-1(d) it was done after increasing the electrical field stepwise up to 400 kV/cm, due to little response at 200 kV/cm. For each sample (a-e) of Figure 4.16 the P-E (*i*), I-E (*ii*) and S-E (*iii*) response is shown. Frequency dependence shows that on a general basis the P_r decreases with the frequency while the E_c seems to largely increase as the frequency descend. In sample P-Pow-1 the P-E loops show some asymmetry at 100 Hz. The P-E loops of sample P-Pow-2(*e_i*) become distinctly more round at lower frequency, indicating that larger leakage current contributes at lower frequency. Generally for all samples, the current density peak flattens and the field at which occur throughout cycle decrease upon lowering the frequency and the strain loops show some asymmetric behaviour at high frequency.

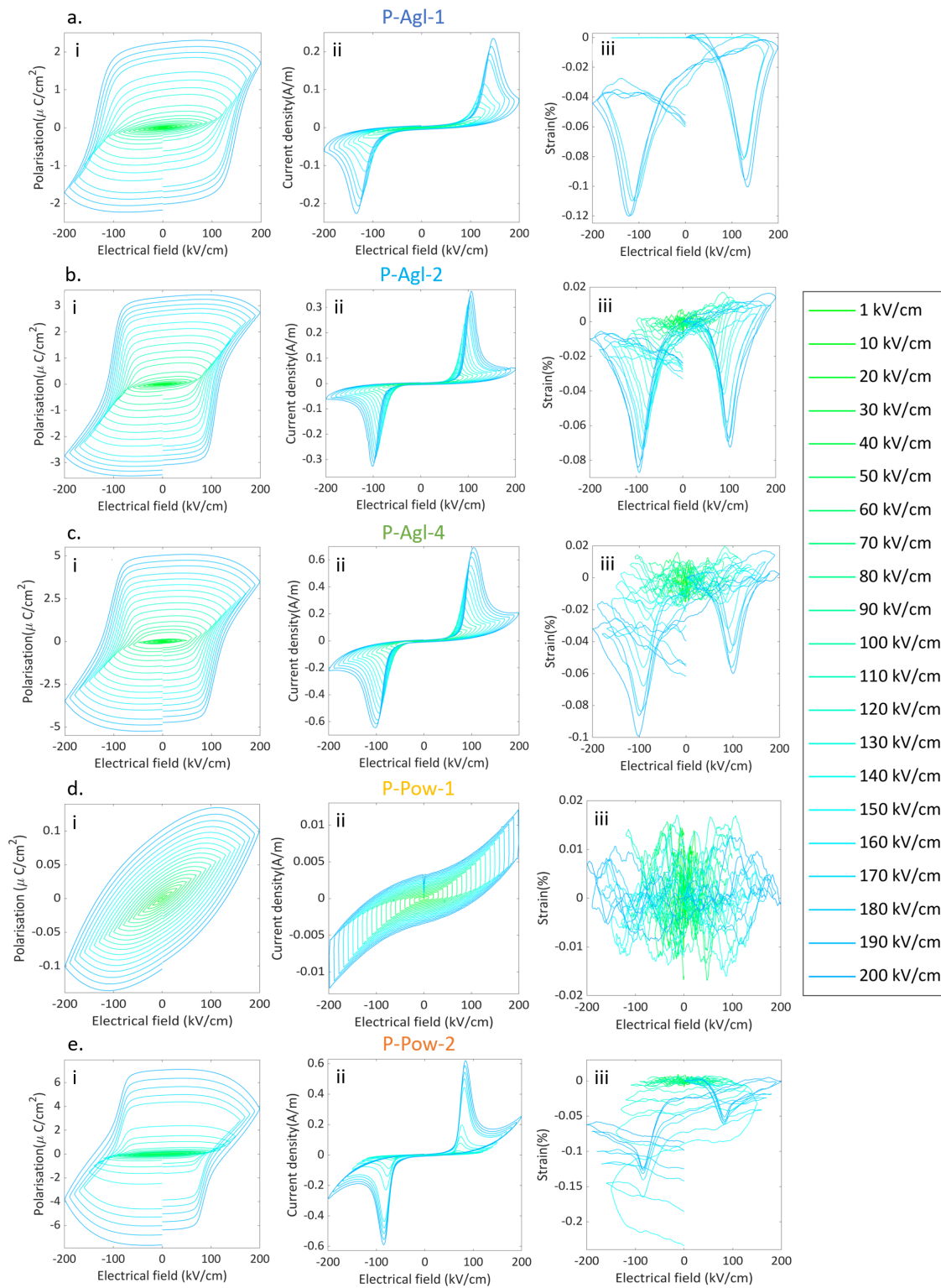


Figure 4.15: P-E(*i*), I-E(*ii*) and S-E(*iii*) data for the samples a: P-Agl-1, b: P-Agl-2 c: P-Agl-4, d: P-Pow-1 and e: P-Pow-2, while being cycled with stepwise increased electric fields up to 200 kV/cm.

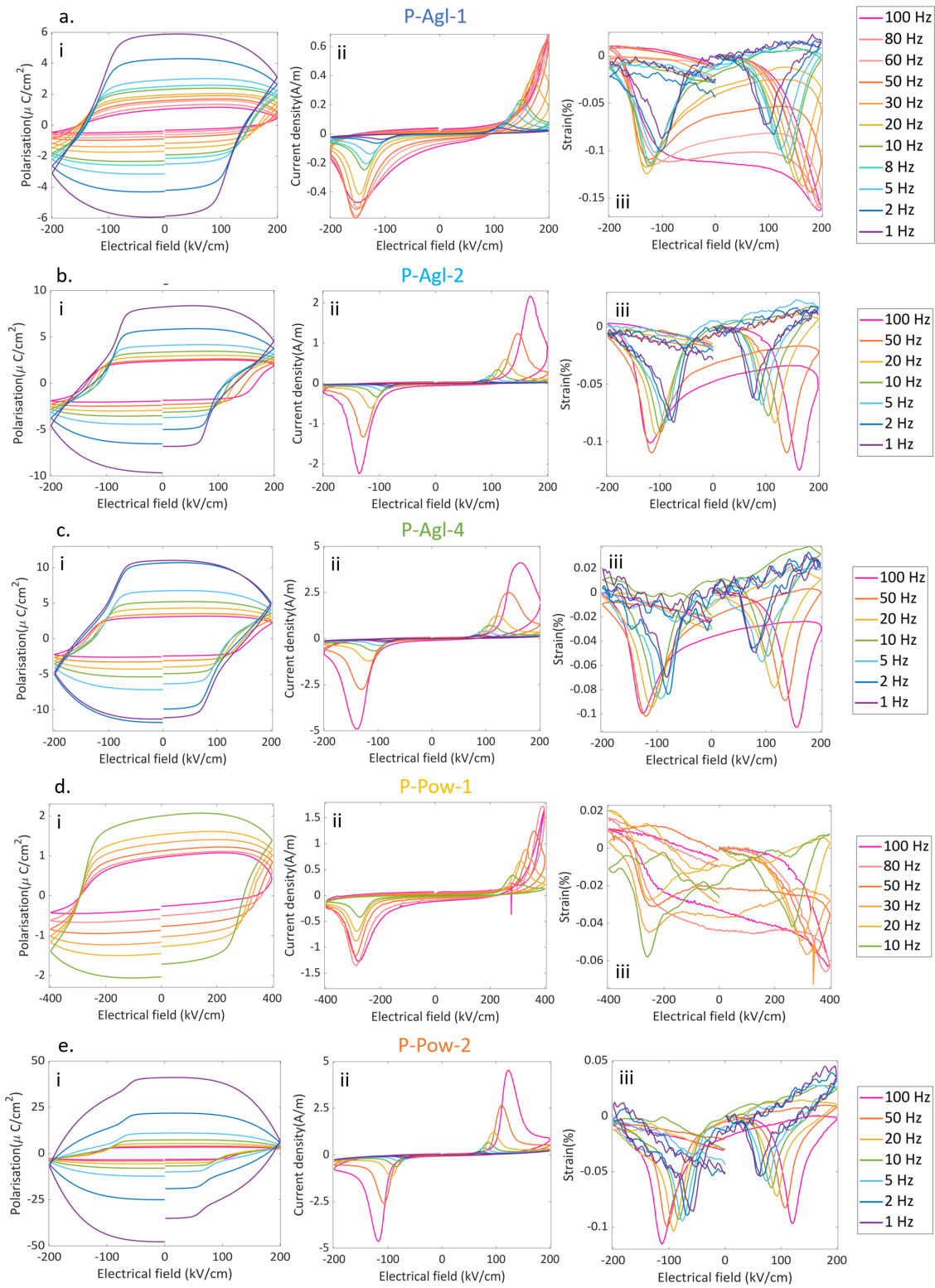


Figure 4.16: P-E(i), I-E(ii) and S-E(iii) data for the samples a: P-Agl-1, b: P-Agl-2 c: P-Agl-4, d: P-Pow-1 and e: P-Pow-2, while being cycled at 200 kV/cm (P-Pow-1 cycled 400 kV/cm) while the electrical field frequency was varied between 100 and 1 Hz.

5 Discussion

The main results presented are related to the sample microstructure, structural phase composition and electrical properties of crushed agglomerate powder (C-Pow), pressed agglomerate samples (P-Agl) and pressed powder samples (P-Pow) of the plastic crystal compound TMAFeBrCl_3 . Thus, the discussion will be broken into three sections: Sample microstructure, structural phase determination and electrical properties.

5.1 Sample microstructure

The fracture surface examination showed that the microstructure of both types of pressed samples appear to represent a fracture surface of a brittle material, such as ceramics, as there are no signs of plastic deformation, like ductile tearing. A second observation is that the microstructure appear to be of high density, without pores, which indicates that plastic deformation through hot pressing of these plastic crystals enable easy formation of dense polycrystalline materials. From the grain size differences observed in the optical images of the pressed agglomerate and pressed powder samples it was expected that the SEM images would show microstructural difference between the samples as well. On the contrary, the SEM images show that the three main features observed, smooth and rough surfaces as well as flat looking areas, are present in both of the two types of samples. Thus, the SEM image analysis were not able to support the grain size difference of the pressed agglomerate and powdered samples nor between the two pressed samples. The details regarding optical and SEM images which led to this conclusion is discussed in the two following paragraphs.

The optical images of the pressed samples clearly show that the pressed powder samples have a higher density of grain boundaries, visible due to translucency of the sample and that the light is refracted at them. This indicates that the pressed powder samples have smaller average grain size than the samples pressed from agglomerates (Figure 4.2). Signs for grain size difference in the two types of samples were further investigated by SEM of fracture surfaces of two pressed agglomerate samples, P-Agl-1 and P-Agl-2, along with two pressed powdered samples, P-Pow-1 and P-Pow-3. It is conventional to estimate grain size from micrographs of polished microstructure surfaces by using the intercept method [38, 39]. However, due to solubility of the materials studied, a typical approach for polishing or etching was not possible and no new method have been developed to prepare such surfaces of the pressed samples investigated in this project. Thus, a solely qualitative examination of the microstructure using the fracture surfaces from both types of pressed samples have been carried out.

There were three significant features observed at the fracture surfaces of the four pressed samples, P-Agl-1, P-Agl-2, P-Pow-1 and P-Pow-3. These were smooth surfaces, rough and more textured surfaces and flat looking areas. Smooth surfaces (marked in green) were observed in all the samples, as can be seen in Figure 4.5 (a_{iii}), 4.6 (a_{ii} and a_v), 4.7 (a_{ii} and b_{iii}), as well as 4.8 (b_{ii}) for the samples P-Agl-1, P-Agl-2, P-Pow-1 and P-Pow-3, respectively. This could be indicative of along grain boundary (intergranular) fracture[19]. The rough textured surfaces (marked with blue) shown in the Figure 4.5 (a_{iv} , a_v , a_{ii} , b and c) for sample P-Pow-1 and in Figure and 4.7 (a_{ii} and b_{ii}), can originate from the fracture happening through the bulk of the grains, as transgranular cracking, giving a texture decided by the crystal lattice and not the microstructure of the sample. This is preferred in larger grains [19]. Flat looking areas (marked in yellow) were observed in all the samples, as can be seen in Figure 4.5 (b_i , c d_i and d_{ii}), 4.6 (a_{iii}), 4.7 (a_{ii}), as well as 4.8 (a_i , a_{ii} and a_{iii}) for the samples P-Agl-1, P-Agl-2, P-Pow-1 and P-Pow-3, respectively. The flat areas observed

in P-Agl-1 (Figure 4.5 (b_i, c)) are of different character than the rest of the flat looking areas. They appear to be even and smooth, with scratch like lines going in various directions on the sample. There is a possibility that these areas are created by mechanical pressing during sample preparation for SEM images. However, they could also potentially be preexisting boundaries that have remained during hot pressing, and that have acted as points of high level of stress concentration, making a fracture occurring along these boundaries. The other flat looking areas could be caused by brittle fracture along a crystallographic plane [19], tiny grains merging during hot pressing or simply along grain boundaries of large grains.

5.2 Characterisation of majority phase

Literature shows that TMAFeBrCl_3 has a series of polymorphic phase transitions between -25 and 200 °C. The transition into the mesophase is the highest temperature transition occurring at 110 °C [23]. Our previous work [1] has shown that certain synthesis conditions give rise to coexistence of the two solid state phases that are present below the mesophase, Amm2 and Cmcm, at room temperature. This was based on comparison of work carried out by Walker [25, 29], and Harada et al. [23] to the experimental work done in [1], which are distinguished by a different number of crystallisation and recrystallisation steps used during synthesis. This previous work shows that on cooling the Cmcm to Amm2 phase transition temperature occurs close to room temperature, but that a slight lowering of the transition onset, from 30 to 25 °C, in various batches of crystals occur. This was used as an explanation for observed phase coexistence, because with lowered transition onset, the phase transition from Cmcm to Amm2 phase would not be allowed to be driven to completion as the samples initially were only cooled to room temperature.

To further explore what effect synthesis and processing have on the structural phase composition, a comparison between samples of pressed agglomerates and pressed powder (crushed agglomerates) was carried out. The comparison reveals that the variation in phase composition also are susceptible to microstructural features such as grain size. Despite not being able to pinpoint microstructural difference between the two types of samples from the SEM study, the optical images suggest that there is a variation in grain size and thus also microstructure. This is supported by the XRD results that suggest that a phase difference between the two types of samples is present. The crushed agglomerate powders are purely Amm2, meaning that no phase coexistence occur before hot pressing is performed. After pressing both the pressed agglomerates and pressed powder samples show some degree of phase coexistence between Amm2 and Cmcm phase, however the two types of samples differ in terms of phase compositional ratio, and preferred phase. The hot pressed powder samples turn out as majority Cmcm phase, where the amount of Amm2 present do not exceed 12 wt%. For the pressed agglomerate samples the phase compositional ratio show more variation (Table 4.1), given by two majority Amm2 samples, one majority Cmcm (48 wt% Amm2) sample and one sample of unidentified majority phase. Thus, the XRD results indicate that the pressed powder samples are more susceptible to get 'stuck' in the Cmcm phase than the pressed agglomerate samples. From this observation it could be suggested that the thermal excursion used during pressing (i.e. up to 125 °C), and thus the thermal history might be responsible for the phase coexistence. Alternatively it could be the influence of residual stress remaining in the structure after pressing causing the phase coexistence. The last-mentioned being implicated by the distinguishable difference in phase assemblage of the two samples, as different microstructures are thought to likely result in different residual stress states, as seen in plastic deformation of metals [40–42].

The DSC data support the XRD results. First by showing that the Cmc_m to Amm2(II-III) transition on cooling occurs at 25 °C, as suggested by previous work [1]. Secondly, the DSC data confirms the difference between the two types of pressed samples. One supporting observation is that the Amm2 to Cmc_m (III-II) transition, on heating, has lower peak intensity and smaller area under the curve for the Cmc_m majority samples P-Pow-1 and P-Pow-2, than for the assumed Amm2 majority samples C-Pow-2 and P-Agl-1. The area under the curve represents the total enthalpy of the transition, which again could be related to the mass of material transitioning, meaning that less amount of Amm2 phase transition into Cmc_m phase, in the majority Cmc_m phase samples, supporting that the samples are majority Cmc_m [43, 44]. However, the conclusion reached in previous work, being that the only reason the transition into Amm2 was not driven to completion was that the cooling was naturally stopped at room temperature, is not supported equally. The DSC thermal cycle first went from room temperature to -25 before cycling to 200 °C, meaning that if the conclusion from previous work were to hold, no difference would be distinguishable for the two types of samples. On the contrary, such a difference is observed. Furthermore, the entropic and enthalpic difference seen in the Amm2-Cmc_m phase transition, between the different type of samples, does not substantially change with increased number of cycles. This reveals that the mechanism responsible for phase coexistence is not easily relaxed with repeated heat treatment, but rather represent a more permanent feature of the sample structures. While the kinetics of the transition might play a role, meaning the heating rate could impact phase coexistence, this does not explain the observed difference between the two types of samples. This leaves the most likely explanation to be residual stress resulting from hot uniaxial pressing that would be different in the pressed agglomerate and pressed powder samples.

Raman and IR spectroscopy was performed to collect information that could support XRD results. The IR data give additional comparative data for the two types of pressed samples. There are parts of the results that support the XRD data, in terms of there being differences between the assumed majority Amm2 and majority Cmc_m samples. This is evident by the presence or lack of presence of bands at 2924 and 2961 cm⁻¹ in the pressed agglomerate and pressed powder samples, respectively. However the fact that the Amm2 majority phase sample P-Agl-2 and the Cmc_m majority phase sample P-Pow-2 both show peaks (unidentified) at 887 cm⁻¹, which is not present in the other two samples, could argue for phase similarities in P-Agl-1 and P-Pow-2, while the many unidentified signals that are only present in P-Pow-2 could argue that this was a completely different phase all together. Thus, further studies are necessary to link the temperature dependent changes to specific crystallographic phases in the material.

Raman spectroscopy was carried out as a temperature study in order to allow looking at differences of the various phases in one single sample and thus avoiding some ambiguity created by factors related to sample preparation. The two shoulders at 206 and 294 cm⁻¹ (Figure 4.10 b) decrease in intensity with increased temperature. The intensity change observed could be related to the transition from orthogonal Amm2 phase to centrosymmetric Cmc_m phase. As the transition leaves the overall structure symmetric it is likely that perturbations of the complex ion FeBrCl₃⁻, from its perfect tetragonal structure, could be relaxed and thus have reduced the intensity of the two shoulders [35]. For the bands at the higher wavenumber range, related to the organic cation, there is a broadening observed in the band at 2924 cm⁻¹ which is indicative that a change of symmetry in the system has occurred between the two temperatures[34]. It can also be observed that the baseline of the average temperature spectra shift to higher intensities with increased temperatures. Even though some trends related to increasing temperature and thus presumably the phase change

occurring in the material are identified, further analysis is needed to link these with molecular dynamics in the different structural phases.

Anomalies were observed in the results achieved for the P-Agl-4 sample. The XRD pattern was difficult to interpret as all peaks below $18\ 2\Theta$ were either suppressed or shifted, by about 10° . While some shift of peaks in the XRD diffractograms can be explained by residual strain from pressing, this is not observed in such a large extent in any of the other samples. The XRD pattern was reproduced, meaning that the lack of diffraction lines is a real feature, but except for the P-Agl-4 being somewhat thinner than the other samples, no other physical trait that could cause this behaviour has been identified. In addition to potential residual stress in the sample, a possible explanation is that the sample shows preferred orientation, leading to suppression of some diffraction lines. DSC show that the Amm2-Cmcm transition in P-Agl-4 resembles the transition seen in the Cmcm majority P-Pow-2 and P-Pow-3 samples, while the electrical properties, and distinctly S-E behaviour in the field dependent data resemble that of the other pressed agglomerate samples, which were both majority Amm2. If trusting the DSC results, supporting Cmcm phase majority of sample P-Agl-4, the ferroelectric behaviour could also be explained by the previously proposed field induced transition into the Amm2 phase. This also indicates that the different strain behaviour observed in the two pressed powder samples is caused by the different microstructure and not the difference in initial phase composition. Thus, comparing all data collected from the P-Agl-4 sample (XRD, DSC and electrical measurements) one can conclude that the P-Agl-4 sample is likely to be majority Cmcm.

5.3 Electrical properties

Looking at the hysteresis data, which yields information about the materials functional properties, the perhaps main observation of this study is that there is an overall trend for all five samples measured. This show that all the samples mostly have typical ferroelectric characteristic in terms of P-E, I-E and S-E behaviour. Some differences with respect to magnitude of E_c , P_r , S_{PP} and I_{Peak} for the various samples are present. The TMAFeBrCl₃ plastic crystals in current work show large E_c , in the range of 116-150 kV/cm and low P_r , between 2.2-7 $\mu\text{C}/\text{m}^2$, at field strengths of 200 kV/cm, compared to bulk perovskite materials where the observed E_c is between 0.5-150 kV/cm and P_r is from 20-50 $\mu\text{C}/\text{m}^2$ [14]. However, the behaviour is rather comparable to findings in the studies by Harada et al. [23] and Walker et al. [26]. These overall trending is seen both in the field and frequency dependent studies. As some of the samples are majority Cmcm phase, which is centrosymmetric and thus not ferroelectric, this is unexpected. This suggests that a field induced transition, into the non-centrosymmetric and ferroelectric Amm2 phase, is occurring for those samples. However, such a transition, often visible in the field hysteresis loops, as discussed in section 4.6.2, is not evident in the data [14, 17].

The general strain behaviour show relatively large S_{PP} , around 0.1%, but which is comparable to the other previous studies on TMAFeBrCl₃ [1, 25, 26]. Most of the loop has negative value. Such strain shapes, with mostly negative strain occurring on switching, have earlier been observed in single crystals and textured ceramics [14]. In single crystals this has been known to follow residual stresses in the structure, while in textured materials, it follows from the specific types of domains that are present. Thus, if polarisation directions that hold more negative strain contribute most, the strain loops will be mostly negative. As the pressed samples studied here, is of polycrystalline nature, the effect of specific domains is most relevant as an explanation, and it is therefore believed

that the pressed samples are textured [14, 18]. In previous work by Walker et. al. it is suggested that texturing or preferential crystallographic orientation can occur during pressing, this is also supported by wider observation of uniaxially hot pressed ceramics. Because of this it is assumed that it is likely to also occur in the samples studied in current work, although the multiphase nature of the materials studied complicates the XRD profiles and makes orientation difficult to identify with any certainty. It is yet unknown how the texture is influenced by the plastic flow that happens during hot pressing, but further investigation to determine the preferred orientation would be interesting.

In the frequency dependent study, the strain loops show asymmetry at high frequency which is likely to be due to incomplete reversal of the domains upon switching, which again is caused by time dependency and would be largely promoted by defects present in the material [25, 45]. All the five samples generally show similar behaviour as a function of frequency, however the rounding of the P-E loop of the P-Pow-2 sample at low frequency is distinct. This is a sign of higher leakage current being present [3, 14, 25] in the sample and fits well with the large change observed in the current-voltage measurement before and after cycling.

All the samples measured exhibited electric field dependent degradation of their resistance. It appears that the effect is more pronounced in the pressed powder samples, and the largest change is observed in the P-Pow-2 sample. Studies [25, 46] suggests that defects can be more mobile at grain boundaries in halide perovskites. Mobile defects and impurities that accumulate at grain boundaries upon cycling, and by their movement contribute to leakage currents in the sample, are a possible explanation to why the pressed powder samples, with smaller grains and more grain boundaries, show higher degradation of resistivity. The two pressed powder samples P-Pow-1 and P-Pow-2 show differences in the leakage current behaviour. As the two sample were pressed from C-Pow-1 and C-Pow-2, respectively, and no standardised crushing procedure was utilised, the grain size of the two samples can vary. Looking closely at the optical images (Figure 4.2) the crystal grain size appear to be smaller for P-Pow-1 than P-Pow-2. This is not consistent with expectations, as the sample with the larger grain size show the largest change in leakage current upon cycling. This may be related to the additional drying which was carried out on C-Pow-1 before pressing, reducing the amount of moisture in the sample. As previously mentioned the strain behaviour of the pressed powder samples also differ somewhat from the pressed agglomerate samples. For sample P-Pow-1 the field dependent study shows strain loops without typical ferroelectric behaviour, however a S-shaped curve is repeated. A similar S-shape is initially observed in the P-Pow-2 sample, but in this sample, it stabilises into the ferroelectric characteristic butterfly strain loop at higher field strengths. The S-shape could also be related to drift of ions within the structure, however the mechanisms linking electromechanical strain and leakage are complex and beyond the scope of this study.

When comparing P-E behaviour of the two samples (Table 4.4), with grain size difference in mind, the larger E_c and lower P_r observed for P-Pow-1 correspond to behaviour expected from literature [14]. Namely, suggesting that a smaller grain size will cause the effect observed due to more pinning of domain walls at grain boundaries. However, as a phase transition is suggested to take place, residual stress is believed to be present in the sample and electrical leakage is observed, it is difficult to distinguish the exact role of the grain size in the samples.

6 Conclusion

This project has been carried out with the overall goal of gaining better insight on the novel plastic crystal class of ferroelectrics. To accomplish this the synthesis-structure-property relationship of the promising ferroelectric plastic crystal TMAFeBrCl_3 was investigated. First, a microstructural study of samples with different grain size was constructed by preparing two types of pressed samples; from pressed agglomerates and from pressed powder (crushed agglomerates). Differences in the microstructure were identified through investigation of optical images and SEM micrographs of the two types of samples. Furthermore, the structural phase of the two sample types were determined by XRD. Techniques such as DSC, Raman and IR were employed to gain confirmation and broader insight to the information gained by the XRD data. DSC can give insight to the mechanisms behind phase transition and which phases are present at what temperature, while vibrational spectroscopy can yield information about molecular vibration and rotation in the material. Finally, the functional properties and how they are affected by variations in the microstructure and structural phase composition were investigated through current-voltage and field dependent hysteresis measurements. The main results of the overall study are as follows:

- Optical images of the pressed samples suggest that the pressed powder (P-Pow) samples have higher grain boundary density, and thus smaller average grain size than the pressed agglomerate (P-Agl) samples. While the qualitative SEM analysis of fracture surfaces could not help identify specific differences between the two types of samples.
- XRD results, mostly supported by DSC and IR, suggest that the P-Pow samples were more susceptible to end up having the centrosymmetric and non-ferroelectric Cmcm phase as majority phase than the P-Agl samples. Further, the DSC suggest that the difference is related to residual strain remaining after uni-axial hot pressing.
- Electrical properties suggest that all samples show similarly trending ferroelectric behaviour regardless of structural phase composition, indicating that, even not specifically observed, the centrosymmetric Cmcm -majority samples must experience field induced transitions into the non-centrosymmetric $\text{Amm}2$ phase.

The aim of this study was to investigate the synthesis-structure-property relationship of the promising ferroelectric plastic crystal. This study has given new information about the plastic crystal ferroelectric TMAFeBrCl_3 , and thus provided insight to the broader class of plastic crystal ferroelectrics in general.

7 Further work

The research on plastic crystals ferroelectrics is limited in general, and further investigation is required to reveal the full potential of this novel material class. Potential ways to further explore TMAFeBrCl_3 are as follows.

- Raman measurements of a Cmcm majority phase sample at room temperature would allow a conclusion of the temperature series of the Amm2 majority phase sample.
- Temperature dependent IR spectroscopy study would complement Raman, as well as make better grounds to draw conclusions such that confirmation bias could be avoided.
- Temperature dependent XRD would allow a phase comparison without the impact of factors which may vary between different samples, such as for example strain and orientation.
- Develop a method for polishing fracture surfaces of pressed samples of TMAFeBrCl_3 .
- Develop a method to do phase characterisation before and after electrical measurements so that it would be possible to confirm the field induced transitions that must occur in the Cmcm majority samples when cycling at increasing fields.
- Conduct a study which focuses on the vulnerability of the structural phase of the hot pressed TMAFeBrCl_3 samples. This could include further investigation of the synthesis conditions and pressing procedure, investigation of orientation in pressed samples and powder, both before and after (grind up samples again) pressing, as well as phase determination of pressed samples before and after cycling at increasing field strengths.

References

- [1] N. S. Løndal, *Improving synthesis of ferroelectric plastic crystal tetramethylammonium bromotrichloroferrate*, Coursework report, TMT4510 Nanotechnology Specialisation project (NTNU), 2019.
- [2] G. H. Haertling, “Ferroelectric ceramics: history and technology”, *Journal of the American Ceramic Society*, vol. 82, no. 4, pp. 797–818, 1999.
- [3] D. Damjanovic, “Ferroelectric, dielectric and piezoelectric properties of ferroelectric thin films and ceramics”, *Reports on Progress in Physics*, vol. 61, no. 9, p. 1267, 1998.
- [4] J. Timmermans, “Plastic crystals: a historical review”, *Journal of Physics and Chemistry of Solids*, vol. 18, no. 1, pp. 1–8, 1961.
- [5] A. H. King, “Our elemental footprint”, *Nature materials*, vol. 18, no. 5, p. 408, 2019.
- [6] Dept of Electronic Engineering, Graduate School of Engineering, Tohoku University, *Illustrative image from article “Super-Flexible Liquid Crystal Device for Bendable and Rollable Displays”*, https://www.tohoku.ac.jp/en/press/flexible_liquid_crystal_device.html, [Online; accessed 10-July-2020], 2016.
- [7] T. Ibn-Mohammed, C. A. Randall, K. Mustapha, J. Guo, J. Walker, S. Berbano, S. Koh, D. Wang, D. Sinclair, and I. Reaney, “Decarbonising ceramic manufacturing: A techno-economic analysis of energy efficient sintering technologies in the functional materials sector”, *Journal of the European Ceramic Society*, vol. 39, no. 16, pp. 5213–5235, 2019.
- [8] G. H. Haertling, “Ferroelectric thin films for electronic applications”, *Journal of Vacuum Science & Technology A: Vacuum, Surfaces, and Films*, vol. 9, no. 3, pp. 414–420, 1991.
- [9] J. Schmitz, “Low temperature thin films for next-generation microelectronics”, *Surface and coatings technology*, vol. 343, pp. 83–88, 2018.
- [10] I.-C. Cheng and S. Wagner, “Overview of flexible electronics technology”, in *Flexible Electronics*, Springer, 2009, pp. 1–28.
- [11] C. A. Randall, N. Kim, J.-P. Kucera, W. Cao, and T. R. ShROUT, “Intrinsic and extrinsic size effects in fine-grained morphotropic-phase-boundary lead zirconate titanate ceramics”, *Journal of the American Ceramic Society*, vol. 81, no. 3, pp. 677–688, 1998.
- [12] Y. Tan, J. Zhang, Y. Wu, C. Wang, V. Koval, B. Shi, H. Ye, R. McKinnon, G. Viola, and H. Yan, “Unfolding grain size effects in barium titanate ferroelectric ceramics”, *Scientific Reports*, vol. 5, p. 9953, 2015.
- [13] Y. Su, H. Kang, Y. Wang, J. Li, and G. J. Weng, “Intrinsic versus extrinsic effects of the grain boundary on the properties of ferroelectric nanoceramics”, *Physical Review B*, vol. 95, no. 5, p. 054121, 2017.
- [14] L. Jin, F. Li, and S. Zhang, “Decoding the fingerprint of ferroelectric loops: comprehension of the material properties and structures”, *Journal of the American Ceramic Society*, vol. 97, no. 1, pp. 1–27, 2014.
- [15] R. J. Tilley and R. Tilley, *Understanding solids: the science of materials*. Wiley Online Library, 2004, ch. 11 Insulating solids.
- [16] Y. A. Genenko, J. Glaum, M. J. Hoffmann, and K. Albe, “Mechanisms of aging and fatigue in ferroelectrics”, *Materials Science and Engineering: B*, vol. 192, pp. 52–82, 2015.

- [17] D. Berlincourt, H. Krueger, and B. Jaffe, "Stability of phases in modified lead zirconate with variation in pressure, electric field, temperature and composition", *Journal of Physics and Chemistry of Solids*, vol. 25, no. 7, pp. 659–674, 1964.
- [18] A. D. Moriana and S. Zhang, "Lead-free textured piezoceramics using tape casting: A review", *Journal of Materiomics*, vol. 4, no. 4, pp. 277–303, 2018.
- [19] W. Callister Jr, *Materials science and engineering: an introduction*. John Wiley & Sons, 2007, ch. 8 Failure.
- [20] J. Timmermans, "Researches in stoichiometry. I. The heat of fusion of organic compounds", *Bull. soc. chim. Belg*, vol. 44, pp. 17–40, 1935.
- [21] R. Brand, P. Lunkenheimer, and A. Loidl, "Relaxation dynamics in plastic crystals", *The Journal of chemical physics*, vol. 116, no. 23, pp. 10 386–10 401, 2002.
- [22] J. M. Pringle, P. C. Howlett, D. R. MacFarlane, and M. Forsyth, "Organic ionic plastic crystals: recent advances", *Journal of Materials Chemistry*, vol. 20, no. 11, pp. 2056–2062, 2010.
- [23] J. Harada, N. Yoneyama, S. Yokokura, Y. Takahashi, A. Miura, N. Kitamura, and T. Inabe, "Ferroelectricity and piezoelectricity in free-standing polycrystalline films of plastic crystals", *Journal of the American Chemical Society*, vol. 140, no. 1, pp. 346–354, 2017.
- [24] J. Harada, T. Shimojo, H. Oyamaguchi, H. Hasegawa, Y. Takahashi, K. Satomi, Y. Suzuki, J. Kawamata, and T. Inabe, "Directionally tunable and mechanically deformable ferroelectric crystals from rotating polar globular ionic molecules", *Nature chemistry*, vol. 8, no. 10, p. 946, 2016.
- [25] J. Walker, R. Miranti, S. L. Skjærvø, T. Rojac, T. Grande, and M.-A. Einarsrud, "Supercoercive electric field hysteresis in ferroelectric plastic crystal tetramethylammonium bromotrichloroferrate (iii)", *Journal of Materials Chemistry C*, vol. 8, no. 9, pp. 3206–3216, 2020.
- [26] J. Walker, S. Scherrer, N. S. Løndal, T. Grande, and M.-A. Einarsrud, "Electric field dependent polarization switching of tetramethylammonium bromotrichloroferrate (III) ferroelectric plastic crystals", *Applied Physics Letters*, vol. 116, no. 24, p. 242 902, 2020.
- [27] A. Biswas, A. Priyadarsini, and B. S. Mallik, "Dynamics and Spectral Response of Water Molecules around Tetramethylammonium Cation", *The Journal of Physical Chemistry B*, vol. 123, no. 41, pp. 8753–8766, 2019.
- [28] Z. Czaplá, O. Czupiński, Z. Galewski, L. Sobczyk, and A. Waśkowska, "Successive phase transitions in tetramethylammonium tetrachloroferrate (III)", *Solid state communications*, vol. 56, no. 8, pp. 741–742, 1985.
- [29] Various unpublished work supervised by J. Walker, including the internal report: M. Andrianarisoa, *Synthesis and characterization of tetramethylammonium bromotrichloroferrate (III) ferroelectric plastic crystals*, 2019.
- [30] M. Döbbelin, V. Jovanovski, I. Llarena, L. J. C. Marfil, G. Cabañero, J. Rodriguez, and D. Mecerreyes, "Synthesis of paramagnetic polymers using ionic liquid chemistry", *Polymer Chemistry*, vol. 2, no. 6, pp. 1275–1278, 2011.
- [31] G. Bottger and A. Geddes, "The infrared spectra of the crystalline tetramethylammonium halides", *Spectrochimica Acta*, vol. 21, no. 10, pp. 1701–1708, 1965.

- [32] J. T. Edsall, "Raman spectra of amino acids and related substances III. Ionization and methylation of the amino group", *The Journal of Chemical Physics*, vol. 5, no. 4, pp. 225–237, 1937.
- [33] M. A. Hossain, F. Ahmed, and J. Srivastava, "A raman spectroscopic study of tetramethylammonium tribromocadmate", *physica status solidi (a)*, vol. 151, no. 2, pp. 299–304, 1995.
- [34] A. Caretta, R. Miranti, R. W. Havenith, E. Rampi, M. C. Donker, G. R. Blake, M. Montagnese, A. O. Polyakov, R. Broer, T. T. Palstra, *et al.*, "Low-frequency Raman study of the ferroelectric phase transition in a layered CuCl 4-based organic-inorganic hybrid", *Physical Review B*, vol. 89, no. 2, p. 024301, 2014.
- [35] K. Nakamoto, "Infrared and Raman Spectra of Inorganic and Coordination Compounds", *Handbook of Vibrational Spectroscopy*, 2006.
- [36] Q. Zhao, T. S. Herng, C. X. Guo, D. Zhao, J. Ding, and X. Lu, "Thermoresponsive magnetic ionic liquids: synthesis and temperature switchable magnetic separation", *RSC advances*, vol. 6, no. 19, pp. 15731–15734, 2016.
- [37] E. Spinner, "Raman-spectral depolarisation ratios of ions in concentrated aqueous solution. The next-to-negligible effect of highly asymmetric ion surroundings on the symmetry properties of polarisability changes during vibrations of symmetric ions.: Ammonium sulphate and tetramethylammonium bromide", *Spectrochimica Acta Part A: Molecular and Biomolecular Spectroscopy*, vol. 59, no. 7, pp. 1441–1456, 2003.
- [38] H. Abrams, "Grain size measurement by the intercept method", *Metallography*, vol. 4, no. 1, pp. 59–78, 1971.
- [39] W. Callister Jr, *Materials science and engineering: an introduction*. John Wiley & Sons, 2007, ch. 4.11 Grain size determination.
- [40] I. Gutierrez-Urrutia and D. Raabe, "Grain size effect on strain hardening in twinning-induced plasticity steels", *Scripta Materialia*, vol. 66, no. 12, pp. 992–996, 2012.
- [41] R. Armstrong, I. Codd, R. Douthwaite, and N. Petch, "The plastic deformation of polycrystalline aggregates", *The Philosophical Magazine: A Journal of Theoretical Experimental and Applied Physics*, vol. 7, no. 73, pp. 45–58, 1962.
- [42] H. Conrad, "Grain size dependence of the plastic deformation kinetics in Cu", *Materials Science and Engineering: A*, vol. 341, no. 1-2, pp. 216–228, 2003.
- [43] E. Moukhina, "Enthalpy calibration for wide DSC peaks", *Thermochimica acta*, vol. 522, no. 1-2, pp. 96–99, 2011.
- [44] M. Brown, "Determination of purity by differential scanning calorimetry (DSC)", *Journal of Chemical Education*, vol. 56, no. 5, p. 310, 1979.
- [45] U. Robels and G. Arlt, "Domain wall clamping in ferroelectrics by orientation of defects", *Journal of Applied Physics*, vol. 73, no. 7, pp. 3454–3460, 1993.
- [46] Y. Yuan and J. Huang, "Ion migration in organometal trihalide perovskite and its impact on photovoltaic efficiency and stability", *Accounts of chemical research*, vol. 49, no. 2, pp. 286–293, 2016.

A Complementary figures

A.1 CRR processing of Raman data

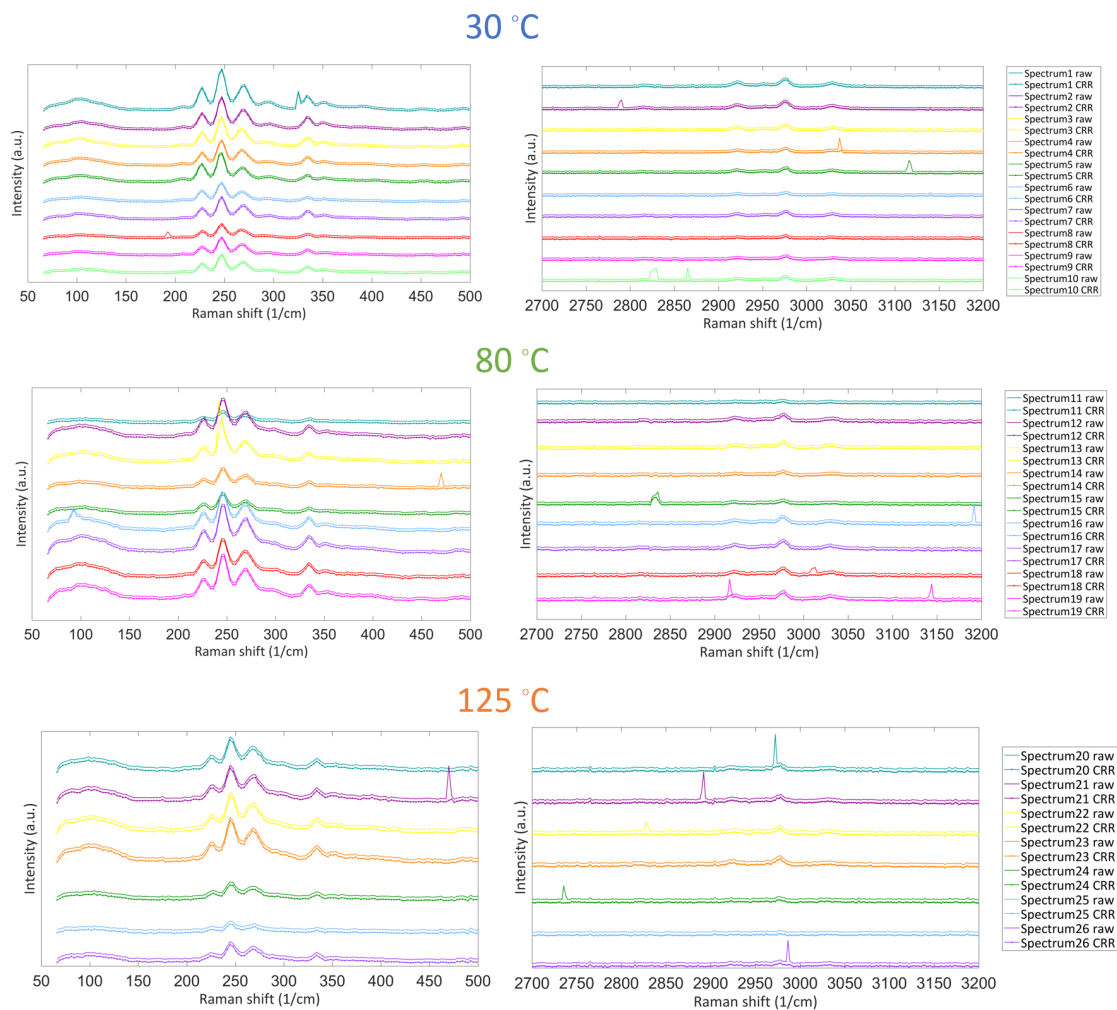


Figure A.1: Full set of spectra used in temperature dependent Raman study. The data with unfilled markers belong to before CRR processing, while the filled belong to CRR processed spectra.

A.2 P-E, I-E and S-E hysteresis curves at maximum field

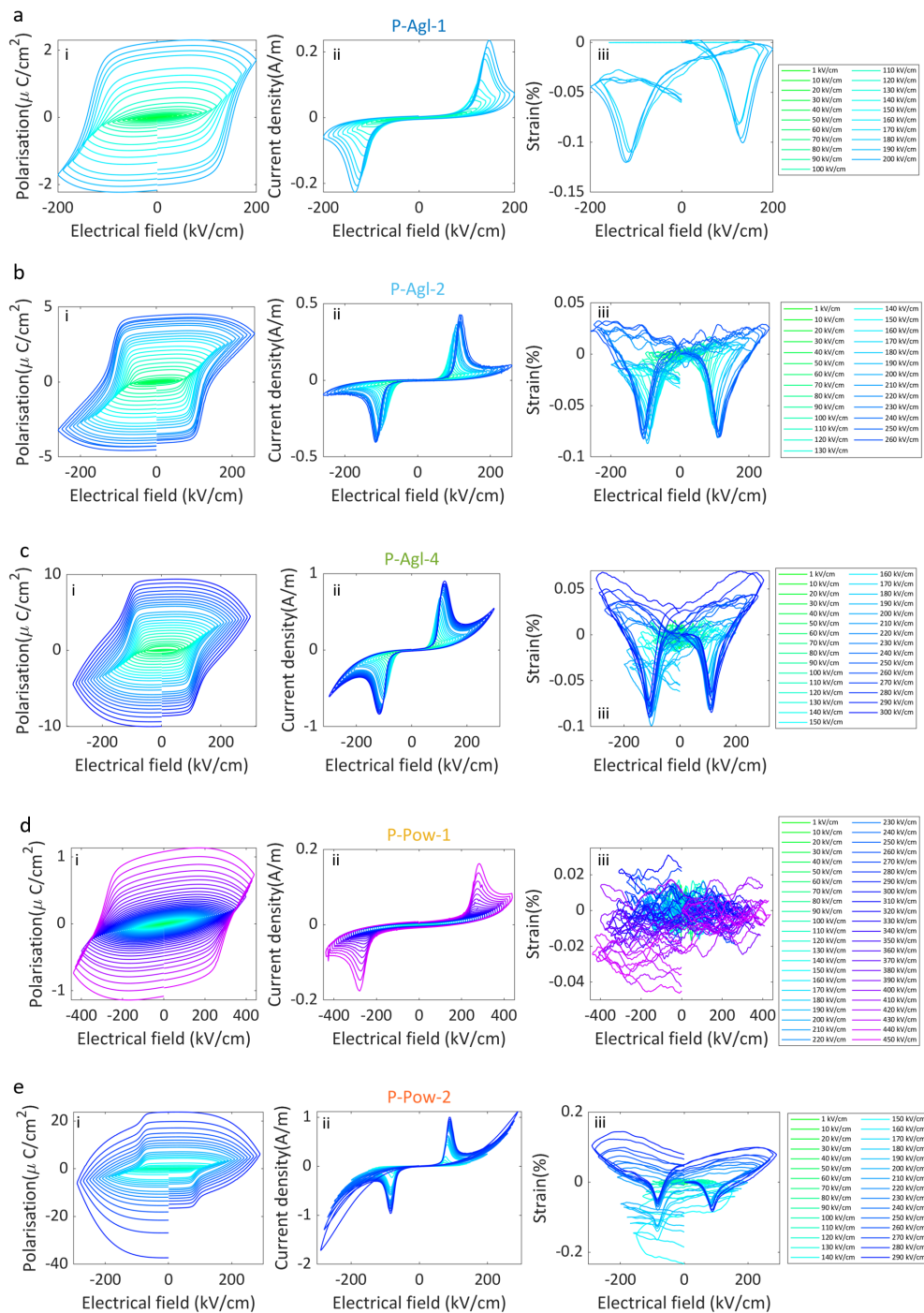




Figure A.2: P-E(*i*), I-E(*ii*) and S-E(*iii*) data for the samples a: P-Agl-1, b: P-Agl-2 c: P-Agl-4, d: P-Pow-1 and e: P-Pow-2, while being cycled with stepwise increased electric fields up to maximum field.

B Risk assessment

| NTNU | | Hazardous activity identification process | | | | Number | Date |  |
|--|--|---|---------------------------|--|------------------------|---|------------|---|
|  | | | | | | HMSRV2601 | 22.03.2011 | |
| HSE | | | | | | Page | Replaces | |
| | | | | | | | 01.12.2006 | |
| Unit: (Institute) | | IMA | | | | Date: 27.04.2020 | | |
| Line manager: | | Tor Grande | | | | | | |
| Participants in the identification process (incl. function): <small>(supervisor, student, co-supervisor, others)</small> | | Mari-Ann Einarsrud, Julian Walker, Nora Løndal | | | | | | |
| Short description of the main activity/main process: | | Synthesis of tetramethylammonium tetrachloroferrate(III)-based plastic crystals. Raman spectroscopy of synthesised crystals | | | | | | |
| Is the project work purely theoretical? (YES/NO) | | No | | | | | | |
| <i>Answer "YES" implies that supervisor is assured that no activities requiring risk assessment are involved in the work. If YES, skip rest of the form.</i> | | | | | | | | |
| Is the project work safe to perform outside normal work hours (8-17)? (YES/NO) | | Yes | | | | | | |
| Responsible supervisor: | | Julian Walker, Mari-Ann Einarsrud | | | | Student: Nora Statle Løndal | | |
| ID nr. | Activity/process | Responsible person | Existing documentation | Existing safety measures | Laws, regulations etc. | Comment | | |
| 1 | Preparing aqueous solutions of organic and inorganic precursors, mixing and dehydrating the mixed solution. | Nora Statle Løndal | HSE risk assessment 30721 | PPE, fume hoods and ventilation on rotary evaporator | n/a | Gloves, lab coat and safety glasses and fume hood required | | |
| 2 | General risk associated with crystal and pressed pellet sample handling (preparation for pressing, drying, XRD, Raman, IR and SEM imaging) | Nora Statle Løndal | | PPE, fume hoods | n/a | Gloves, lab coat and safety glasses and fume hood required | | |
| 3 | Hot uniaxial pressing of crystals at <250°C and <50 MPa | Nora Statle Løndal | HSE risk assessment 30723 | PPE and engineering control on furnace (front protective door) | n/a | Gloves, lab coat and safety glasses and engineering controls (front door) to be used | | |
| 4 | Drying of samples in vacuum drying oven. | Nora Statle Løndal | | | n/a | Glove, lab coat and safety glasses required. Venting of vacuum chamber before opening it. Using heat protection gloves when taking samples out at elevated temperatures. | | |
| 5 | Raman spectroscopy of crystals/pressed samples | Nora Statle Løndal | | | | Engineering controls on the equipment prevent exposure of the naked eye to the laser beam. The equipment safe work procedures establish procedures to prevent operator exposure to laser | | |
| 6 | Infrared spectroscopy of crystals/pressed samples | Nora Statle Løndal | | | | Engineering controls on the equipment prevent exposure of the naked eye to the laser beam. The equipment safe work procedures establish procedures to prevent operator exposure to laser | | |
| 7 | Temperature dependent XRD | Nora Statle Løndal | | | | The equipment safe work procedures establish procedures to prevent burns at high temperature. Avoid too high temperature causing degradation of material and exposure to harmful vapour. | | |
| 8 | Lab work during Covid-19 restrictions | Nora Statle Løndal | | | | Follow the health government and NTNU guidelines for routines for using lab during the Covid-19 situation: Wash hands when entering/ leaving lab, keep recommended distance to other lab users, wash surfaces you have been in contact with with 70-80% ethanol before leaving lab. Stay home if experiencing symptoms for Covid-19. To prevent being in close contact with other people, when student need training on equipment, engineer will be asked to perform measurements instead of giving training. | | |

| | | | | | | |
|---|------------------------|--|--|-----------|------------|---|
| NTNU | Risk assessment | | | Number | Date |  |
|  | | | | HMSRV2603 | 04.02.2011 | |
| HMS /KS | | | | Page | Replaces | |
| | | | | | 09.02.2010 | |

Unit: (Institute)

Line manager:

IMA

Date:

27.04.2020

Participants in the identification process (incl. function): _____

(supervisor, student, co-supervisor, others)

Risk assessment of:

Signatures:

Synthesis of tetramethylammonium tetrachloroferrate(III)-based plastic crystals. Raman spectroscopy of synthesised crystals

Responsible supervisor: Mari-Ann Einarsrud, Julian Walker Student: Nora Statle Løndal

| ID nr. | Activity from the identification process form | Potential undesirable incident/strain | Likelihood: | | Consequence: | | Risk value (human) | Comments/status Suggested measures |
|--------|--|---|-------------|-------|-------------------|------------------|--------------------|---|
| | | | (1-5) | Human | Environment (A-E) | Economy/material | | |
| 1 | Preparing aqueous solutions of organic and inorganic precursors, mixing and dehydrating the mixed solution. | Breathing hazardous organic precursor dust. | 1 | B | B | A | B1 | The weighing of organic precursors MUST be conducted in a fume hood - This reduces the risk of inhalation of dangerous dust to ZERO |
| 1 | | Spilling dilute aqueous | 2 | A | A | A | A2 | Solutions may irritate skin and damage eyes. |
| 1 | | Breathing fumes or burns during dehydration process | 1 | A | A | A | A1 | Solutions may irritate skin and damage eyes, thus PPE - Gloves, lab coat and glasses MUST be worn at all times. |
| 2 | General risk associated with crystal and pressed pellet sample handling (preparation for pressing, drying, XRD, Raman, IR) | Skin irritation due to touching of crystals/pressed pellets | 1 | A | A | A | A1 | Gloves, lab coat and safety glasses must be worn during handling of samples |
| 2 | | Eye irritation if get into eyes | 1 | A | A | A | A1 | Gloves, lab coat and safety glasses must be worn during handling of samples |
| 2 | | Dangerous if swallowed or breathed in | 1 | B | A | A | B1 | Work under fume hood when preparing crystal powder samples. |
| 3 | Hot uniaxial pressing of crystals at <250°C and <50 MPa | Skin irritation due to touching of crystals and burns when removing and placing samples in the hot press. | 2 | A | A | A | A2 | Gloves, labcoat and safety glasses must be worn during this procedure. Gloves prevent skin contact with crystals and a labcoat protects arms from contact with hot press plates. Users must use tweezers to remove sample from press to avoid burning hands. |
| 4 | Drying of samples in vacuum drying furnace | Dangerous to breath in vapour formed in vacuum chamber. | 1 | A | A | A | A1 | Chamber should be vented before opened |
| 5 | Raman spectroscopy, temperature dependent study | Laser radiation can cause eye injury | 1 | B | A | A | B1 | Should avoid looking directly into laser. Engineering controls on the equipment prevent exposure of the naked eye to the laser beam. |
| 5 | | Laser radiation can cause skin burn | 1 | A | A | A | A1 | Avoid exposure of skin to laser radiation. The equipment safe work procedures establish procedures to prevent operator exposure to laser |
| 5 | | Risk of burn at elevated temperatures | 1 | A | A | A | A1 | Safe work procedures will be followed with each set up, minimizing risk of burns. |
| 5 | | Harmful vapour from sample degradation | 1 | B | A | A | B1 | Temperature must be kept under 200 degrees C |
| 6 | Infrared Spectroscopy | Laser radiation can cause eye injury | 1 | B | A | A | B1 | Should avoid looking directly into laser. Engineering controls on the equipment prevent exposure of the naked eye to the laser beam. |
| 6 | | Laser radiation can cause skin burn | 1 | A | A | A | A1 | equipment safe work procedures establish procedures to prevent operator exposure to |
| 7 | Temperature dependent XRD | Harmful vapour from sample degradation | 1 | B | A | A | B1 | Temperature must be kept under 200 degrees C |
| 7 | | Risk of burn at elevated temperatures | 1 | A | A | A | A1 | Safe work procedures will be followed with each set up, minimizing risk of burns. |
| 8 | Use of lab 036 for SEM Imaging | Risk of infection of Covid-19 | 1 | B | A | A | B1 | Only come to the lab if symptom free. Book lab time and follow restriction of number of people in the lab; 1 person. Wash hands when entering the lab, and when leaving the lab. Wipe off surfaces, equipment, handles which the person has come in contact with; using (70-80%) ethanol. |
| 8 | IR Spectroscopy/Hading over samples to engineer. | Risk of infection of Covid-19 | 1 | B | A | A | B1 | Arrange with engineer how to hand over samples without coming close to each other. Use gloves when handling sample holders etc. Wipe of sample holders with ethanol after being in contact with them. |

| value = Likelihood | Criteria | Consequence | | | | | |
|-----------------------|-------------------------------------|-------------|-----------------|--|---|------------------------------|--|
| | | Grading | | Human | Environment | Economy/material | |
| Likelihood | Minimal: Once every 50 year or less | E | Very critical | May produce fatality/ies | Very prolonged, non-reversible damage | Shutdown of work >1 year. | |
| Value | Low: Once every 10 years or less | D | Critical | Permanent injury, may produce serious health damage/sickness | Prolonged damage. Long recovery time. | Shutdown of work 0.5-1 year. | |
| 1 | Medium: Once a year or less | C | Dangerous | Serious personal injury | Minor damage. Long recovery time | Shutdown of work < 1 month | |
| 2 | High: Once a month or less | B | Relatively safe | Injury that requires medical treatment | Minor damage. Short recovery time | Shutdown of work < 1week | |
| 3 | Very high: Once a week | A | Safe | Injury that requires first aid | Insignificant damage. Short recovery time | Shutdown of work < 1day | |
| 4 | | | | | | | |
| 5 | | | | | | | |

| | | | | | | |
|-------------|-----------------|-----|--------|------|-----------|----|
| CONSEQUENCE | Very critical | E1 | E2 | E3 | E4 | E5 |
| | Critical | D1 | D2 | D3 | D4 | D5 |
| | Dangerous | C1 | C2 | C3 | C4 | C5 |
| | Relatively safe | B1 | B2 | B3 | B4 | B5 |
| | Safe | A1 | A2 | A3 | A4 | A5 |
| | Minimal | Low | Medium | High | Very high | |
| | LIKELIHOOD | | | | | |

| | |
|-------------|---|
| | Description |
| Explanation | Unacceptable risk. Safety measures must be implemented. |
| Color | Measures to reduce risk shall be considered. |
| Red | Acceptabel risk. |
| Yellow | |
| Green | |

